applied sciences

MDPI

Article

Fluid-Rock Interaction Signature in Palomares Fault Zone—New Mineralogical and Geochemical Insights into the Tectono-Magmatic Águilas Arc Geothermal System (SE Spain)

Elena Real-Fernández [1,2,*], Manuel Pozo [3,*], Cristina De Ignacio [2], Ángel Sánchez-Malo [1], Enrique Sanz-Rubio [1] and Luis Villa [4]

[1] Geomnia Natural Resources, SLNE, 28400 Collado Villalba, Madrid, Spain; asanchezmalo@geomnia.es (Á.S.-M.); esanz@geomnia.es (E.S.-R.)
[2] Department of Mineralogy and Petrology, Complutense University of Madrid, 28040 Madrid, Spain; cris@ucm.es
[3] Department of Geology and Geochemistry, Autonomous University of Madrid, 28049 Madrid, Spain
[4] Minersa Group, 48992 Getxo, Biscay, Spain; luis.villa@minersa.com
* Correspondence: elenreal@geomnia.es (E.R.-F.); manuel.pozo@uam.es (M.P.)

Featured Application

Fault segment studies provide a deeper understanding of fluid circulation processes related to the exploration and characterization of geothermal systems, as they are ideal areas for examining geological, geochemical, and hydrogeological alterations.

Abstract

The southeastern Iberian Peninsula, particularly the Águilas Arc within the Neogene Volcanic Province (NVP), represents a promising geothermal domain with complex tectonics and geology. The Palomares Fault Zone (PFZ), a key shear structure initiated during the Late Miocene, acts as a conduit for fluid migration, promoting mineralization and potential anomalies of rare and critical metals through fluid–rock interaction. This study investigates such interactions in the southernmost Águilas Arc, focusing on the El Arteal fault segment within the eastern PFZ strand. Mineralogical, geochemical, and hydrogeological analyses were performed using XRD, SEM, and ICP-MS techniques. Results reveal six mineral assemblages (MA) within the fault segment where the fault gouge samples were characterized by cataclastic textures and the occurrence of authigenic minerals, including halite, kaolinite, illite, paragonite, goethite, hematite, gypsum, barite, celestine, and quartz. Geochemical data indicate enrichment signatures in large-ion lithophile elements (LILE) and minor chalcophile and light rare-earth elements (LREE). Two thermal hydrofacies with alkaline metals enrichment were identified in wells and mine shafts: (1) $Na^+SO_4^{2-}$ and (2) Na^+Cl^-, where the latter exhibits high Na^+ and Cl^- concentrations toward deeper sectors. These findings suggest multiple stages of fluid–rock interaction controlled by temperature: an early phase dominated by epithermal mineralization, followed by late-stage circulation of hypersaline fluids. This evolution provides an abnormal geochemical signature that is unique in the Aguilas Arc Geothermal System.

Keywords: fault rocks; fluid–rock interactions; hydrothermal-geothermal fluids; brine waters; mineralogy; trace elements geochemistry

Academic Editor: Nikolaos Koukouzas

Received: 24 December 2025
Revised: 27 January 2026
Accepted: 28 January 2026
Published: 30 January 2026

1. Introduction

The assessment of mineral resources in geothermal brine waters associated with hydrothermal systems, both in magmatic and non-magmatic settings, has emerged as a strategic approach to address the increasing demand for rare and critical metals, which are essential to advanced technologies and renewable energy applications [1–3]. These geothermal systems are characterized by distinctive hydrochemical signatures, often marked by anomalies in highly mobile elements such as Li, Rb, Cs, and B. These anomalies are primarily attributable to extensive fluid–rock interaction during the evolution of hydrothermal processes [4,5]. Despite their potential, exploration of these systems remains highly capital-intensive [6]. Recent research emphasises the dual value of geothermal projects. In addition to the exploitation of geothermal energy from thermal waters, hypersaline hydrothermal deep fluids have the potential to serve as a promising source of critical metals for high-tech industries [2,7]. The distribution and concentration of these elements are strongly controlled by temperature gradients, fluid composition, and host lithology, factors that determine mineralisation potential [2,8]. The tectonic and structural framework also plays a fundamental role in controlling the migration and reactivity of geothermal fluids within the reservoir. These fluids are known to predominantly ascend along fault zones, driven by pressure gradients and contrasts in permeability [9–13]. In magmatic-hydrothermal systems, the presence of these fluids is attributed to magmatic exsolution during the cooling and crystallisation of magma chambers [14,15]. During their ascent, these fluids commonly mix with infiltrated meteoric waters, generating complex geochemical environments conducive to metal enrichment and/or neoformation of authigenic phyllosilicates/clay minerals in faulted rocks and their surrounding areas [16–21]. Notable examples of brine waters indicative of magmatic–geothermal systems include the Salton Sea geothermal field (USA), El Tatio field (Chile), and Campi Flegrei and Cesano (Italy), whereas other brines connected to non-magmatic-geothermal systems include the Upper Rhine Graben (France and Germany) and the North German Basin [1,2]. Furthermore, recent advances in extraction technologies, such as sorbent-based recovery and kinetic modelling, highlight the feasibility of obtaining critical metals directly from geothermal brines. This reinforces the economic and environmental significance of geothermal systems in the global transition toward sustainable resource management [6,7].

The Águilas Arc (Figure 1a), located in the southeastern region of the Iberian Peninsula (Spain) and developed since the Middle Miocene to the present day [22–26], is recognised as a promising area for geothermal potential [27]. It shows a highly compartmentalized basement architecture resulting from intense Neogene deformation and the development of tectonically-controlled subsiding basins. This configuration is driven by a rigid-plastic indentation process and its association with a vast crustal-scale sinistral wrench zone (the Trans-Alboran shear zone (TASZ) or East Betic Shear Zone (EBSZ)) [22–25]. The indentation was guided since the Middle Miocene by two major shear zones—N20°E sinistral (Palomares–Terreros faults) and N100°E dextral (Las Moreras faults)—under a compressive/transpressive stress field oscillating between NW–SE and N–S (Figure 1a) [22,28,29]. These structures governed magmatic emplacement and hydrothermal circulation. Furthermore, during the Upper Tortonian to Early Messinian, an extensional regime generated crustal fractures and permeability pathways that facilitated the migration of magmatic fluids exsolved during crystallization [22,28]. The arc is located within the NVP, extending from Cabo de Gata (Almería) to Mazarrón–Cartagena (Murcia), with heterogeneous orogenic volcanism: normal and high-K calcalkaline, shoshonitic and lamproitic rocks (middle-to-upper Miocene), and later, Pliocene alkaline basalts [30]. The Murcia–Almería lamproites are the largest and most compositionally variable in the Mediterranean, enriched in Large Ion Lithophile Elements (LILE) and depleted in High Field Strength Elements

(HFSE), with Pb positive anomalies in multielemental diagrams indicative of metasomatized mantle sources [31]. A thinned lithosphere along the SE Iberian margin [32] lifted up terrestrial heat flow, facilitating partial melting and sustaining geothermal systems.

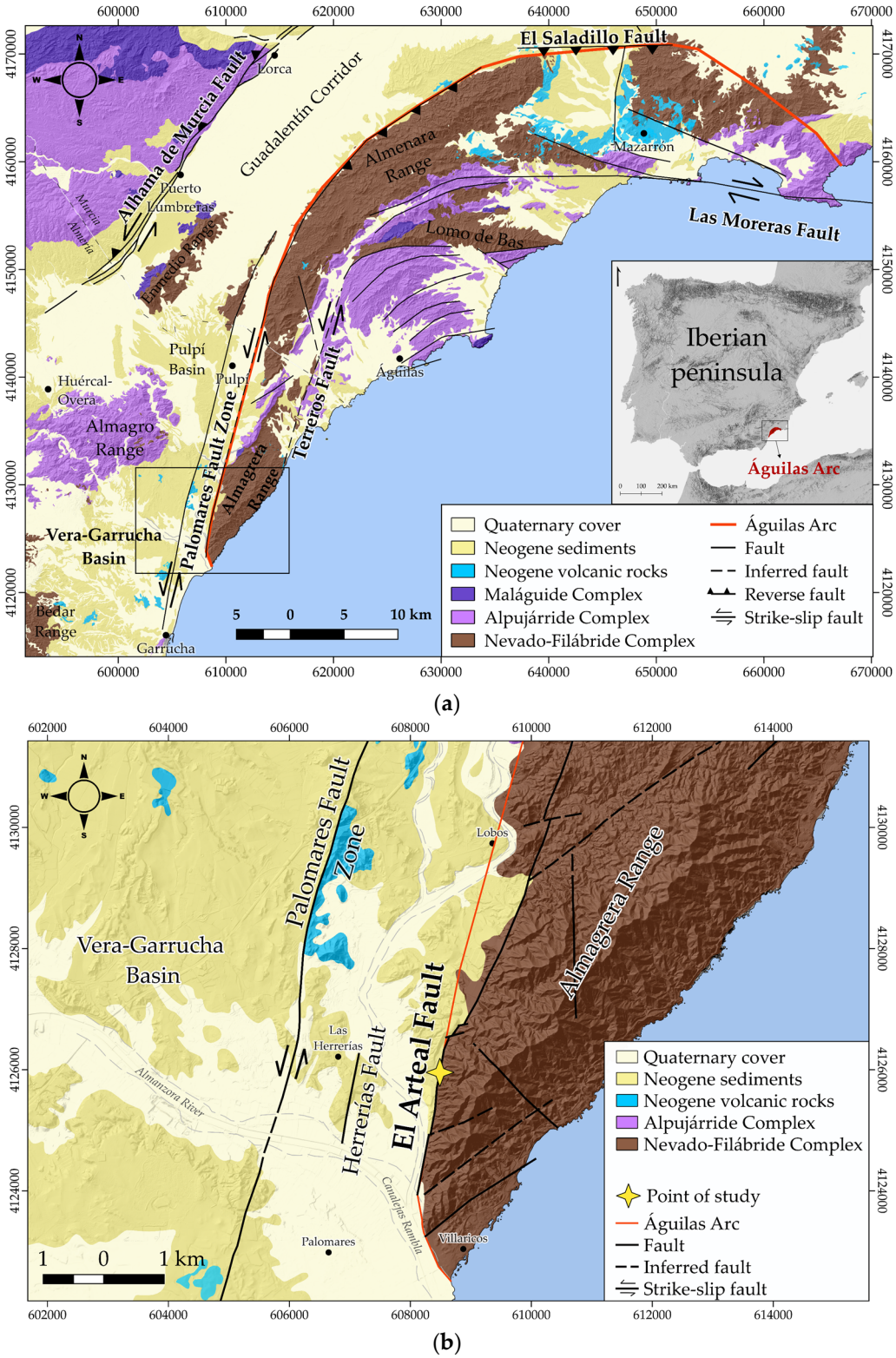

Figure 1. (**a**) The Águilas Arc with the main faults and geological units: The ages of the Nevado-Filábride and Alpujárride complexes range from Paleozoic to Triassic [33]; (**b**) Inset showing the location of the El Arteal fault within the Palomares Fault Zone.

Geothermal studies classify the area as low- to medium-enthalpy, with reservoir temperatures of 60–140 °C at depths of 400–2500 m [34,35], though other estimates suggest 170–190 °C in some cases [36]. These conditions, combined with structural permeability and relatively recent magmatic heat sources, underline the geothermal potential of the Águilas Arc. However, to evaluate the possible extent of it, a thorough knowledge of fluid-rock interaction processes and their bearing on geochemical dispersion patterns of strategic elements is needed. Thus, the objective of this study is to investigate the evidence of such fluid-rock interactions in the southernmost area of the Águilas Arc geothermal system, with a particular focus on the El Arteal segment of the Palomares Fault Zone (PFZ, Neogene) [37,38] (Figure 1b). This segment is regarded as a pivotal location, as it constitutes the primary surface expression through which to examine the mineralogical and geochemical anomalies of faulted rocks and nearby aquifers. These anomalies may be potential indicators of thermal fluid circulation driven by tectono-magmatic activity.

From a metallogenic perspective, the Betic Cordilleras and especially the Águilas Arc, host numerous epithermal polymetallic ore deposits (Pb-Zn-Fe-Ba-Ag-Cu-Sb-Sn), mainly of the vein and manto types, within Paleozoic–Triassic metasediments and Cenozoic volcanic/sedimentary rocks (Cartagena, Mazarrón, Lomo de Bas, Aguilón, Almagrera ranges, amongst others). These deposits are closely associated with high-K calcalkaline and shoshonitic volcanic centers, and regional strike-slip faults that acted as primary conduits for magmatic fluids [39,40]. The PFZ, along with its subsidiary faults El Arteal, Herrerías, and Terreros, is structurally linked to the intense hydrothermal alteration and mineralisation observed within the historical mining districts of the Almagrera Range and Las Herrerías, which is situated within the Vera–Garrucha Basin (Almería). These districts are characterized by abundant quartz, siderite, barite, celestine, and hematite veins, often associated with polymetallic sulphides [18,41,42]. In order to mine the mineral vein deposits (Pb–Ag) in the Almagrera Range, in the vicinity of the Arteal Fault, it was necessary to establish a drainage system due to the presence of groundwater in active mine galleries and shafts. This mining activity revealed the existence of deep brines with temperatures reaching up to 55 °C at depths below 200 m below sea level [36,43,44]. Presently, the El Arteal fault, in conjunction with abandoned shafts and drainage galleries, presents a remarkable opportunity for the study of fluid–rock interaction in geothermal systems.

2. Geological Setting

The southeastern sector of the Iberian Peninsula, particularly the Águilas Arc (Middle Miocene [22,25,26]) in the provinces of Murcia and Almería, is a key segment of the Betic Cordillera, which forms the westernmost part of the Alpine orogenic system in the Mediterranean [23,45]. The Betic Cordillera is characterized by the juxtaposition of the orogenic Internal Zones (Alboran Domain, from bottom to top: Nevado-Filábride, Alpujárride and Maláguide complexes), ranging in age from the Paleozoic to the Early Miocene, and External Zones (Prebetic and Subbetic), range from the Triassic to the Early Miocene [33]. These zones are separated by major tectonic contacts and have been shaped by a complex history of nappe stacking during the Oligocene, Neogene metamorphism, and subsequent Neogene extension and basin formation [23,46,47]. The Águilas Arc is mostly composed of metamorphic Paleozoic and Triassic rocks from the Internal Zones (Nevado-Filábride and Alpujárride complexes), overlain by Neogene–Quaternary marine and continental sediments with thicknesses and facies distribution strongly influenced by tectonic subsidence [23,28,38,48]. The Paleozoic and Triassic metamorphic units include graphitic phyllites and schists, quartzites, and marbles of the Nevado-Filábride and Alpujárride complexes [45,47]. Both units record a Late Cretaceous–Paleogene HP–LT event: the Nevado-Filábride locally reached eclogite facies (omphacite + garnet + phengite ± kyanite ± rutile) [49], whereas

Alpujárride units preserve carpholite-bearing assemblages (~8–10 kbar; ~350–400 °C) [47]. This imprint was largely overprinted during late Paleogene–Miocene extensional exhumation by near-isothermal decompression and recrystallization under amphibolite to upper greenschist facies (~500–550 °C at 4–3 kbar), followed by cooling to ~300–350 °C at 2–1 kbar [47,49,50]. The study is focused on the post-tectonic Vera-Garrucha Basin (Almería) that is mostly composed of Messinian and Pliocene marls delimitated by the Almagro Range (north), the Bédar Range (west), the Cabrera Range (south and southeast of Garrucha), and the Almagrera Range (northeast) (Figure 1a). The basin is strongly asymmetric, and it is highly deformed towards its eastern margin, affected by the Palomares Fault (Almagrera Range) [51–53].

The region also hosts one of the most diverse and well-studied Neogene Volcanic Provinces (NVP) in Europe, with calc-alkaline, high-K calc-alkaline, shoshonitic, ultrapotassic (lamproitic), and alkaline basaltic rocks, with a northward increase in K_2O and incompatible elements, and a decrease in age [30]. Volcanic activity is closely associated with fault zones, with domes, dykes, and sills emplaced along zones of structural weakness.

The tectonic evolution of the southeastern Betics is characterized by a major transition from Alpine compressional tectonics and large-scale nappe stacking during Oligocene to syn- to post-orogenic Miocene extension, followed by a late Tortonian contractional overprint [23,47,49,50,54–56]. During the early Alpine stages, the Internal Zones were subjected to deep burial and high-pressure/low-temperature (HP–LT) metamorphism, locally reaching blueschist to eclogite facies conditions, reflecting their involvement in a continental subduction system [47,57,58]. This compressional phase produced the superposition of the Nevado-Filábride, Alpujárride, and Maláguide complexes as major tectonometamorphic nappes. From Early to Middle Miocene, the geodynamic regime shifted to widespread extension, driven by slab rollback in the Western Mediterranean and the development of low-angle extensional detachments, which facilitated the rapid exhumation of the metamorphic cores [49,50]. This extensional phase led to the doming and tectonic unroofing of the Alpujárride and Nevado-Filábride complexes, ultimately shaping the current structural architecture of the southeastern Betics.

2.1. The PFZ and El Arteal Fault

The PFZ is a major sinistral (left-lateral) strike-slip system formed by several segments with a N10–20°E trend (Figure 1a,b). It is part of the Eastern Betic Shear Zone (EBSZ) and operates as a guide and limit structure that absorbs part of the movement and deformation produced by the tectonic indentation of the Águilas Arc within the EBSZ [22,38,57,59]. The PFZ has been active since the Upper-Tortonian to the Quaternary, and it has a notable dimension, affecting a rock volume of 80 km long, 44 km wide, and 30 km deep [26,38,60]. The PFZ has played a crucial role in the segmentation and migration of Neogene and Quaternary sedimentary depocenters, the uplift and rotation of metamorphic ranges such as the Almagrera Range, and the formation of associated basins (Vera, Pulpí) [38]. Recent gravimetric studies [25] indicate that the PFZ is more segmented and discontinuous than previously thought, with its main trace extending from the Cabrera Range (south of Garrucha) to the southern Pulpí Basin (Figure 1a). Furthermore, PFZ exhibits strike variations in fault kinematics along its trace and tectonic evolution as a result of the need to accommodate compressional tectonic stresses during the Alpine orogenic system [26,38]. In the southern sector (Vera-Garrucha), fault segments dip westward and show an oblique-slip with a significant normal component, promoting subsidence and the development of sedimentary basins such as the Vera Basin. In contrast, in the northern sector (Almenara Range), the same fault segments dip to the east–southeast and display sinistral–reverse kinematics, favouring uplift of the mountain ranges [38].

The El Arteal Fault is a key segment within the eastern and southern strand of the PFZ, bringing into contact the Almagrera Range to the east and the Neogene marine sediments of the Vera-Garrucha Basin to the west (Figure 1b). It is characterized by a sinistral-normal regime striking N10–12°E and dipping 45–86°NW with striae plunging 15–25° southward, and it has been active from the Early Pliocene to the Quaternary [37,38]. El Arteal, together with other segments such as the Terreros and Herrerías faults, accommodates part of the total displacement of the PFZ and plays a crucial role in the tectonic segmentation, uplift, and exhumation of the Almagrera Range [18,38,60]. This structural framework strongly controlled the migration of Neogene and Quaternary depocenters, the development of hydrothermal systems, and the location of ore deposits during the Neogene. The Almagrera Range is an elongated N30°E tectonic block formed by the Nevado-Filábride Paleozoic rocks [61]. The El Arteal fault affects graphite phyllites, mica-schists, and quartzites of the Nevado-Filábride Complex, as well as Mio-Pliocene sands and sandy marls of the Vera-Garrucha Basin.

2.2. Historical Mining

Mining in the Almagrera Range (Figure 1b) revealed one of the most intense hydrothermal activity and mineralisation areas within the region [43]. Mineralisation occurs as lodes and veins mainly in open fracture systems trending N10–40°W in the Almagrera Range, and as stratabound deposits in the Las Herrerías area (Vera-Garrucha Basin). Ore assemblages include galena (often argentiferous), sphalerite, pyrite, chalcopyrite, and sulphosalts (Pb-Sb-Cu-Ag), accompanied by gangue minerals such as quartz, barite, celestite, hematite, and siderite. Silver enrichment typically occurs above the oxidation zone [62–65]. These processes were closely linked to calc-alkaline and shoshonitic volcanism, suggesting a genetic connection between magmatism and hydrothermal ore formation [39,62]. The modern period of mining in the Arteal area began in 1838, following the discovery of the argentiferous galena vein known as the Jaroso lode, and continued until 1957 with alternating phases of activity and abandonment. As mining operations advanced and reached deeper levels, the development of a dewatering system became necessary, so in 1903, two mine shafts were deepened to 250–257 m from the surface (220–227 m below sea level) [44], currently collapsed at 122.5 m from the surface. During its most productive period (1841–1912), the district yielded approximately 500,000 tons of lead and 3000 tons of silver [43]. Moreover, in barite operations near the zone, Minersa mine group yielded between 1993 and 2006 approximately 330,000 tons of Ba-, Sr- and Fe-bearing material [66].

3. Hydrogeological Context

The El Arteal mining activity provided the connection between the thermal Almagrera aquifer and the Vera-Garrucha Neogene aquifer through mine galleries [67,68]. The water pumped out during the mine development was of a geothermal and hypersaline nature, reaching temperatures up to 55 °C at depths close to 200 m below sea level. Furthermore, the pumped brines were characterized by high metal concentration with remarkable contents of Li, K, and Rb [69,70]. In view of the hydromineral economic interest of the brines, the Peñarroya Mining Company constructed an experimental deep well measuring 550 m in depth in 1983. This well was located at the foot of the Almagrera Range, at a distance of 800 m from the Arteal Dewatering System. A series of hydraulic tests was conducted in order to evaluate the feasibility of extracting lithium from brines and the geothermal potential of the area. However, these tests did not yield any conclusive results [36,43,69]. The well was cased to 393 m, below which a slotted-liner casing was installed to 486 m [70].

According to Navarro and Carulla [36], there are two main aquifers in the area, a thermal one hosted in the fractured metamorphic rock (geothermal system of the Almagrera

Range) and another one, the Canalejas alluvial aquifer in the Quaternary and Neogene sediments (Figure 1b). The aquifers exhibit low permeability, resulting in slow recharge by pluviometry. Some researchers have studied this type of water at the El Arteal mine dewatering system, old mine wells in the Almagrera Range, and the experimental deep well. For example, Navarro and Carulla [36] and Navarro [44] determined that the hydrogeological data show Na and Na-Ca chloride dominant facies in all the collected spots with notable Na, K, Ca, Mg, and Li contents (Table 1). They reported that Cl concentrations in this region are higher than those of Mediterranean seawater, and Cl/Br ratios (1564–12,879) show that the elevated salinity cannot be attributed to marine intrusion, as indicated by Cl/Br ratios of approximately 620–660 [71], but rather to the dissolution of halite or the dilution of halite brines. In addition, they estimated a reservoir temperature of approximately 190–200 °C with different geothermometers and a production depth of 2400–3000 m, making the Almagrera Range a potential geothermal resource.

Table 1. Water samples data from Navarro and Carulla [36] and Navarro [43]: El Arteal mine dewatering system, old mine shafts in Almagrera Range (Ramo de Flores, Guzmana), and experimental deep well. Dash (-) indicates that no measurement was taken.

Parameters	El Arteal Mine		Ramo De Flores	Guzmana	Exp. Deep Well	
Data year	1971	1973	1971	1971	1983	1983
Piezometric head (m)	−167	−171.3	−137	−98	−176.8	−195
pH	6.9	3.6	-	2.9	-	-
T(°C)	33	34	35	28	51	51
Salinity (g/L) 110°	10,210	-	40,460	25,130	-	-
Ca (mg/L)	648	830	1400	240	7200	6750
K (mg/L)	134	160	670	197	1700	1750
Mg (mg/L)	282	1180	1035	1244	600	600
Na (mg/L)	2450	1700	9150	4450	28,200	27,400
Cl (mg/L)	3410	3800	1711	8252	58,900	57,500
SO_4 (mg/L)	3275	2500	4300	7575	820	1010
HCO_3 (mg/L)	283	-	0	0	260	260
Br (mg/L)	3.9	-	3.05	1.8	-	-
F (mg/L)	-	2.1	-	-	-	-
Fe (mg/L)	1.9	17.2	206	1400	48	33
Li (mg/L)	6	6.4	27	13.2	65	66
Rb (mg/L)	-	-	-	-	17	18
Zn (mg/L)	-	2.3	-	-	2	1
Si (mg/L)	4	1.7	2	2	6.5	7.1
Sr (mg/L)	-	-	-	-	275	260
Cu (mg/L)	-	1.7	-	-	-	-
As (μg/L)	-	55	-	-	-	-
Ni (μg/L)	-	60	-	-	-	-

4. Materials and Methods

In order to investigate rock–fluid interaction, the fault section was examined through two complementary approaches: The first stage of the research involved the sampling of rocks for petrographic, mineralogical, and geochemical analysis. The second stage involved the collection of water samples from five water wells and mine shafts to assess hydrogeological changes. The abbreviations of methods and additional indicators are located in the subsequent section of the text following the main text.

The fault outcrop is located close to the El Arteal dewatering system due to the area's significance. It extends eight metres and has a wedging morphology, with the upper part being narrower than the lower part. The strike is measured at N12°E, and the dip is 86° to the NW (Figure 2a,b). A total of fifteen rock samples were collected sequentially in the fault outcrop during two field sampling campaigns (September 2023 and May 2024). Three of these samples were taken from the metamorphic and sedimentary rocks outside the fault zone, and thus serve as reference samples. One sample was obtained from phyllites of the Paleozoic Nevado-Filábride Complex (the uplifted block, F1 sample, Figure 2c) with a marked foliation, and the other two samples were obtained from calcareous sands, calcareous sandstone, and sandy marls, which contain microfossils from the Neogene sediments (the downthrown block, F12 and F13 samples). Additionally, twelve samples (F2A–F11) were obtained from the fault core zone, precisely at the contact between these two aforementioned geological units. This zone can generally be classified as foliated fault gouge derived from graphite mica-schists and phyllites with angular clast-supported fine fault breccia, cataclasite and some mylonitic textures (Figure 2d–h). The colour of these materials varies across the segment and was measured with the Munsell scale. The reference sample from the Paleozoic Nevado-Filábride Complex is medium (5B 5/1) to light bluish grey (5B 7/1) (Figure 2c), whereas the foliated fault gouge ranges from dark (N3) and medium dark grey (N4) to dark reddish grey (5R 4/2), greyish- red (10R 4/2) or pale red (5R 6/2) (Figure 2d–g). The black colour is associated with high carbon (graphite) content in these rocks [72]. The Fault gouge in contact with Neogene sediments exhibits similar colours to the reference samples, ranging from pale yellowish brown (10YR 4/2) to dark yellowish orange (10YR 6/6) and greyish orange (10YR 7/4) (Figure 2h).

For petrographic, mineralogical, and geochemical analysis, all rock samples were studied by optical microscopy, X-ray diffraction (XRD), scanning electron microscopy (SEM), and their whole-rock trace elements were obtained by inductively coupled plasma mass spectrometry (ICP-MS).

XRD patterns were obtained both from randomly oriented powders (all samples) and from oriented aggregates (seven representative samples). For the latter, the clay fraction was obtained by dispersion and sedimentation in an aqueous medium according to Stokes' law [73]. After air drying, one of these samples was ethylene glycol solvated, and another one was thermally treated (550 °C) to obtain the oriented aggregates. X-ray diffractograms were obtained with a Bruker D8 Discover (Bruker AXS GmbH, Karlsruhe, Germany) equipped with geometry Theta/2Theta at the Interdepartmental Research Service of the Autonomous University of Madrid (Spain). The X-ray radiation used was CuKα with a wavelength of 1.54060 Å. XRD patterns of randomly oriented powders were performed from 2° to 65° 2θ, while oriented aggregates were analysed from 2° to 30° 2θ, using a step size of 0.02° 2θ and a counting time of 1 s per step. A semiquantitative estimation of the mineral content was carried out using the intensity factors calculated by Schultz [74] and Van der Marei [75].

The petrographic study was performed on eight polished thin sections (30 microns). These samples were impregnated with epoxy before being cut, and subsequently polished with petroleum to prevent disintegration on contact with water. Undisturbed fragments were examined under a Hitachi S-3000N Scanning Electron Microscope (SEM) (Hitachi High-Tech, Tokyo, Japan), after coating with gold (10 nm thick) in a sputtering chamber (Quorum sputter metallization, Q150TS) (Quorum Technologies, Sussex, UK). The SEM has secondary electrons (SE) and Backscattered electrons (BSE) detectors as well as a Quantax Energy Dispersive X-ray spectrometer (EDX), model XFlash 6I30, from Bruker (Karlsruhe, Germany). Resolution was 3 nm at 25kV and voltage from 0.3 to 30 kV.

Whole rock trace elements were analysed using the super trace DL Na_2O_2 fusion (ME-MS89L) and ICP-MS determination analytical protocol at the ALS Global Laboratory Group, S.L in Loughrea, Ireland. 250 g of each sample was pulverized to <75 µm. The results include a selection of lithophile elements such as Li, Be, Mg, Ca and Large Ion Lithophile elements (LILEs: K, Rb, Cs, Sr, Ba), High Field Stress Elements (HFSE: Ti, Nb, Ta, Th, U), Light Rare Earth Elements (LREEs: La, Ce, Pr, Nd, Sm), Middle Rare Earth Elements (MREEs: Eu, Gd, Tb, Dy), Heavy Rare Earth Elements (HREEs: Ho, Er, Tm, Yb, Lu, Y), Transition Trace Elements (TTE: Fe, Mn, V, Co, Ni), other elements (Mo, W, Re, Ga, Ge) and chalcophile elements (Cu, Zn, Ag, Cd, In, Sn, Tl, Pb, Bi, Sb, As, Te, Se).

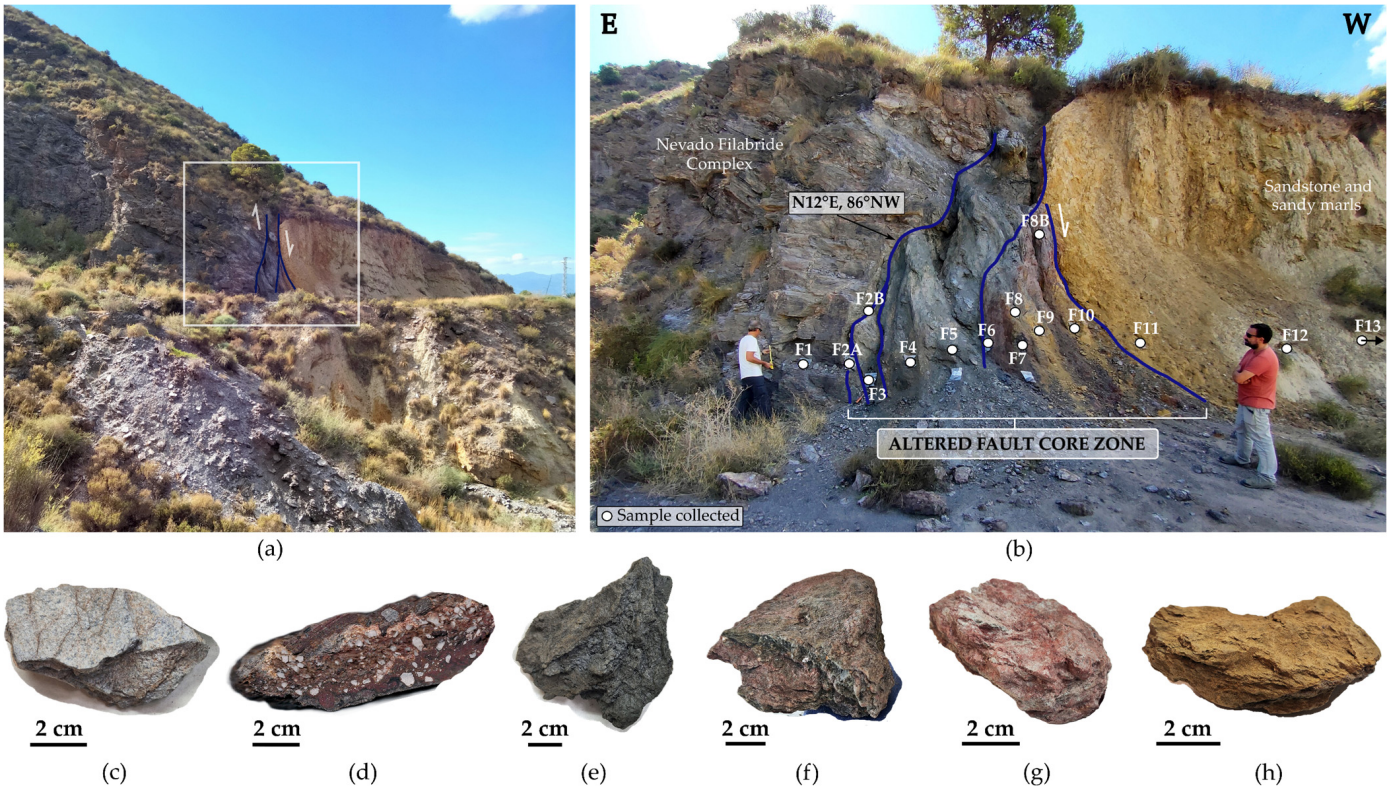

Figure 2. (**a**) Panoramic view of the fault section between the Paleozoic Nevado-Filábride Complex and the Neogene sediments. The arrows indicate the vertical component of slip on the sinistral-normal fault; (**b**) Closer view showing location of samples collected sequentially throughout the fault section. Sampling points indicated by white circles; (**c**–**h**) Details of different and representative samples: (**c**) Sample F2B, which is close to the Nevado-Filábride materials, has a texture similar to the original metamorphic rock and is a light bluish grey colour (5B 7/1); (**d**) Sample F2A exhibits a breccia texture, (**e**–**g**) Samples F3, F7 and F8B are foliated fault gouge with a colour change from dark grey (N4) to greyish red (10R 4/2) and pale red (5R 6/2). Sample F8B has a mylonitic texture; (**h**) Sample F9 is a fault gouge in contact with Neogene sediments and is dark yellowish-orange (10YR 6/6).

To evaluate the composition of the groundwater in the fault-affected area, seven water samples were collected during the same two field campaigns. Five water wells and mine shafts were selected along a transverse profile (SW-NE) to the direction of the studied fault, piercing the geological units of interest (Figure 3a,b). The El Arteal mine dewatering system comprises: one water well (ART-2) and two mine shafts, which are connected by mine galleries (ART3 and ART-4). ART-2 and ART-3 are located in Neogene sediments, whereas ART-4 is situated in the Nevado-Filábride complex. The fourth well, designated ART-1, is utilised for water supply and is located in Quaternary alluvial sediments. The fifth well, labelled S.A., corresponds to the experimental deep well and is located in the Nevado-Filábride complex (Figure 3a,b). All samples were collected at a static level

using a 1-litre stainless steel bailer with a 150 m manual winch for shallow wells and a 500 m automatic winch for deep wells. Temperature, pH, redox potential (Eh; mV), and electrical conductivity (EC; µS/cm) were all measured on-site with a Crison MM40+ portable multimeter device. Standard reference solutions were employed to calibrate the field instrument. Major ions and trace elements were analysed by ICP-MS and Inductively Coupled Plasma-Atomic Emission Spectroscopy (ICP-AES) at the ALS Global Laboratory Group, S.L in British Columbia, Canada.

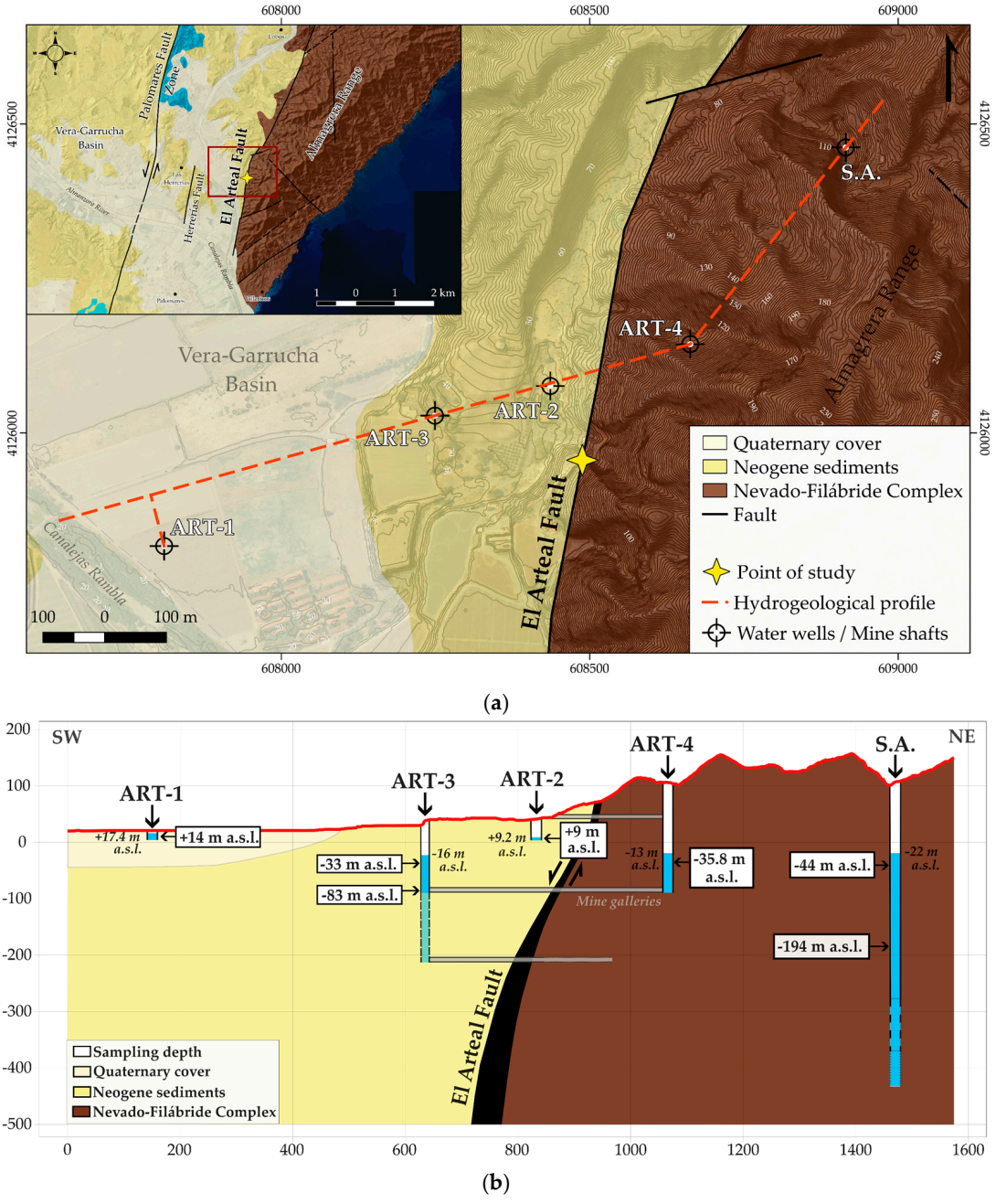

Figure 3. (**a**) Geological map with the location of water wells and mine shafts and the outline of the profile in red. (**b**) Transverse profile (SW-NE) to the direction of the fault and the depth of the water sample taken at the five water wells and mine shafts. ART-1 and ART-2: Wells for water supply; ART-3 and ART-4: El Arteal mine dewatering; and S.A: Experimental Deep Well. Figures in italics show the piezometric head metres above sea level (m a.s.l.) and figures in the white rectangles represent the sampling depth in m above sea level. The grey horizontal lines show the mining galleries that connected the Almagrera thermal aquifer and the Vera-Garrucha Neogene aquifer. Both axes are in metre units. Modified diagram from Gómez Iribarne [68].

5. Results

5.1. Mineralogy

The XRD mineralogical analyses of bulk rock samples indicate a substantial presence of phyllosilicates and quartz throughout the fault zone, in both reference samples and fault core samples. However, other minerals, including halite, gypsum, tridymite, plagioclase, microcline, hematite, rutile, goethite, and carbonates (dolomite, calcite, and/or ankerite) are present in some but not all samples. The proportions of these minerals vary according to sampling location, the type of rock, and the degree of alteration (see Table 2). Phyllosilicates identified in the XRD patterns are mostly dioctahedral micas (muscovite and paragonite), as well as clay minerals, such as illite and kaolinite. Illite/muscovite and kaolinite are the most frequent phyllosilicate minerals in all samples. A small amount of paragonite was further detected in the randomly oriented powders and the oriented aggregates by the (d001) spacing at ~9.63 Å and (d002) spacing at ~4.81 Å in some samples (F5 to F13) of altered fault gouge and breccia. Chlorite was only identified in the randomly oriented powders from three samples, which corresponded to the reference samples from the Neogene sediments (F12 and F13 samples), as well as one sample close to these units (sample F11), by (d001) spacing at 14 Å and (d002) at ~7 Å. In the oriented aggregates, the main identified minerals were illite/muscovite and kaolinite (Figure 4). Additionally, no significant changes were observed between air-dried and ethylene glycol-treated specimens, indicating the absence of expandable layers. Kaolinite was identified by (d001) spacing at 7.14 Å, and illite/muscovite was identified by (d001) spacing at 10 Å, 4.98 Å and at 3.33 Å or 3.31 Å (Figure 4). This slight displacement likely reflects compositional variation and/or minor instrument shift.

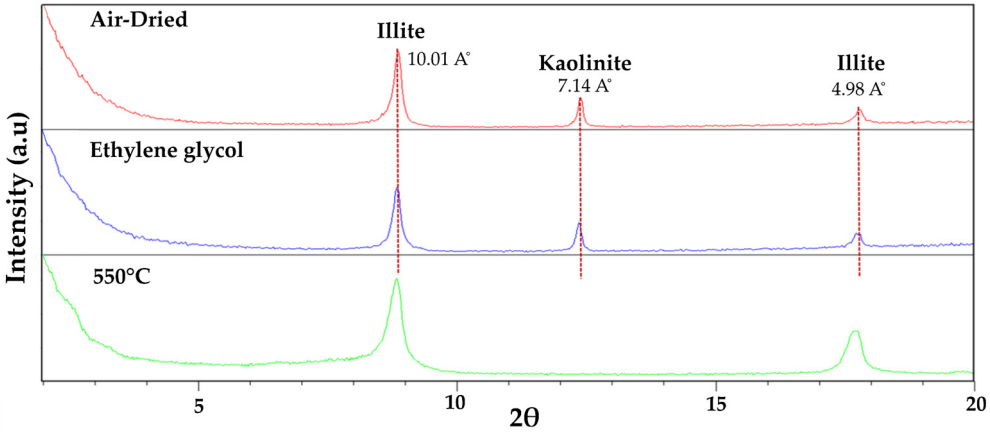

Figure 4. Representative oriented aggregate mounts diffractograms from the sample F2B, with illite and kaolinite.

The semiquantitative analysis in Table 2 shows that the fault gouge and breccia contain a significant increase in phyllosilicates in the central samples of the fault segment, with values reaching up to 64% (F6, Table 2). This is followed by halite, which ranges from 1–2% to a maximum of 10–11%, and gypsum, which is present in small amounts, below 1%. An increase and variation in iron oxides and oxyhydroxides were also observed in the fault core near the Nevado-Filábride Complex reference sample, with goethite values of 8% and hematite values of 14%. The presence of halite and iron oxides/oxyhydroxides is particularly significant, as these minerals are either absent or only scarcely present in the reference samples (F1, F12, and F13). Gypsum, in contrast, is slightly more abundant in the calcareous sands of the Neogene sediments (5%). It is noteworthy that the vast majority of samples lack feldspars, except for fault gouge sample F3 located near the de Nevado-Filábride reference samples (9% Pl + 1% Mc, Table 2). The Fault gouge samples

(F9, F10, and F11) located closest to the Miocene units contain dolomite (up to 6%) and abundant calcite (up to 36%). Rutile, tridymite, and ankerite are occasionally detected but not quantitatively determined. Oriented aggregates were obtained for only five samples (F1, F2B, F5, F5 and F9), as it was not possible to separate the <2 μm fraction in samples F10 and F12. All of these samples contain more than 90% illite and 4–10% kaolinite, with the highest amount of kaolinite found in the fault gouge sample located close to the Nevado-Filábride Complex (F2B + 10% Kln, Table 2).

Table 2. Sample list of El Arteal fault and semiquantification XRD results. Mineral abbreviations according to Whitney and Evans [76]: Ank = Ankerite, Brt = Barite, Cal = Calcite, Clt = Celestine, Chr = Chromite, Dol = Dolomite, Gth = Goethite, Gp = Gypsum, Hl = Halite, Hem = Hematites, Ilt = Illite, Kln = Kaolinite, Mc = Microcline, Mnz = Monazite, PSIc = Phyllosilicates, Pl = Plagioclase, Qz = quartz, Tur = Tourmaline, Trd = Tridymite, Rt = Rutile, Zrn = Zircon. Dash (-) is no data. RS = Reference sample.

		Bulk Sample											Clay Fraction	
Samples	**Type of Rock**	**Qz**	**PSIc**	**Mc**	**Pl**	**Gth**	**Hem**	**Gp**	**Hl**	**Dol**	**Cal**	**Others**	**Ilt**	**Kln**
F1	Phyllite (RS)	71	25	1	-	3	-	-	-	-	-	-	96	4
F2A	Fault breccia	55	30	-	-	1	14	-	-	-	-	-	-	-
F2B	Phyllite altered	68	23	-	2	6	-	-	1	-	-	Rt, Tur, Zrn	90	10
F3	Fault gouge	39	42	1	9	8	-	<1	1	-	-	Rt, Clt, Mnz	-	-
F4	Fault gouge	52	43	-	-	3	-	<1	2	-	-	Brt, Rt	-	-
F5 *	Fault gouge	52	42	-	-	5	-	-	1	-	-	-	96	4
F6 *	Fault gouge	28	64	-	-	3	-	<1	5	-	-	-	-	-
F7 *	Fault gouge	26	49	-	5	1	9	1	9	-	-	Rt, Trd, Mnz, Zrn	93	7
F8 *	Fault gouge	23	53	3	-	6	-	<1	9	6	-	-	-	-
F8B	Mylonitic fault rock	41	51	-	-	-	8	-	<1	-	-	Mnz, Zrn, Tur	-	-
F9 *	Calcareous Fault gouge	23	43	-	-	<1	3	-	8	2	21	Chr, Zrn	91	9
F10 *	Calcareous fault gouge	10	46	-	-	-	-	3	2	3	36	Ank	-	-
F11 *	Calcareous fault gouge	20	33	-	-	-	-	1	11	2	33	-	-	-
F12 *	Calcareous sands (RS)	48	40	2	-	-	-	5	-	3	2	-	-	-
F13 *	Calcareous sandstone and sandy marl (RS)	25	57	-	-	-	-	<1	-	5	5	-	-	-

* Samples where paragonite was identified, but it was not quantitatively determined. Underlining, samples containing chlorite.

Considering the observed mineralogical observations and variations across all samples and their spatial distribution, a total of six distinct MA have been identified: two corresponding to the reference rock samples, and four are associated with the core zone of the fault segment.

- **MA-1** (Nevado-Filábride Complex reference rock (uplifted block): F1 sample). The assemblage is dominated by quartz (71%) and phyllosilicates (25%) with contents below 5% of potassium feldspar and goethite. Phyllosilicates are dominated by illite-muscovite, with traces of kaolinite. The presence of halite was not detected.

- **MA-2** (Fault core: F2A and F2B samples; Figure 5). It is dominated by quartz (55–68%) and phyllosilicates (23–30%) with a relevant content of hematite (1–14%) and goethite (1–6%) together with traces of halite and rutile. Petrographic analysis and SEM observations also identified tourmaline, zircon, plagioclase, and gypsum. Among the phyllosilicates, illite-muscovite and kaolinite were both detected. The study of the clay fraction (<2 μm) revealed contents of 90% illite and 10% kaolinite.
- **MA-3** (Fault core: F3, F4 and F5 samples; Figure 6). It is characterized by a decrease in quartz (39–52%) and an increase in phyllosilicates (42–43%), with variable amounts of goethite (3–8%), plagioclase (0–9%), halite (1–2%), and traces of potassium feldspar. Petrographic analysis and SEM observations also identified the presence of rutile, celestine, monazite, gypsum, and barite. Phyllosilicates are dominated by illite-muscovite and kaolinite, with minor indications of paragonite. The clay fraction (<2 μm) consisted of approximately 96% illite and 4% kaolinite.
- **MA-4** (Fault core: F6, F7, F8 and F8B samples; Figure 7). It is primarily composed of phyllosilicates (49–64%) with a minor amount of quartz (23–41%) with variable contents of goethite (0–6%), hematites (0–9%), halite (traces < 1–9%), dolomite (0–6%), some feldspars (0–5%) and with traces of gypsum. Petrographic analysis and SEM observations additionally have detected rutile, monazite, tourmaline, trydimite, and zircon. Phyllosilicates are dominated by illite-muscovite and kaolinite, with minor indications of paragonite. The clay fraction (<2 μm) consisted of approximately 93% illite and 7% kaolinite.
- **MA-5** (Calcareous fault core: F9, F10, and F11 samples). The assemblage is dominated by phyllosilicates (33–46%), calcite (21–36%), quartz (10–23%), and halite (2–11%). Dolomite, hematite, goethite, and gypsum are present with contents below 5%. SEM observations additionally have detected chromite and zircon. Phyllosilicates identified were illite-muscovite, paragonite, and kaolinite with traces of chlorite. The study of the clay fraction (<2 μm) revealed contents of 91% illite and 9% kaolinite.
- **MA-6** (Neogene sediments (downthrown block): F12 and F13 samples). It is primarily composed of phyllosilicates (40–57%) and quartz (28–45%) and, in amounts equal to or less than 5%, of gypsum, calcite, and dolomite. Phyllosilicates identified were illite-muscovite, paragonite, chlorite, and kaolinite. The presence of halite was not detected.

In the core zone of the fault segment, SEM-EDS observations revealed the presence of neoformed stacked book-like or booklets of kaolinite aggregates, and authigenic quartz in samples from MA-2 and MA-4 (Figure 5a–d). The quartz is euhedral and shows evidence of overgrowth that is enclosed within kaolinite aggregates. In the MA-2 samples, goethite appears as radial aggregates of acicular (Figure 5d) and prismatic crystals, as well as flattened, scale-like formations or botryoidal (globular cluster) (Figure 5e,f). In most of the samples, hematite presents a prismatic morphology infilling pore spaces (Figure 7f) or as tiny spots covering the surface sections of the micas and feldspars in the F7 and F9 samples (MA-4 and MA-5, respectively). Furthermore, other minerals have been identified in the fault gouges, such as zircon, monazite, rutile, acicular celestine, chromite, and barite in MA-2 to MA-5 (Figure 6d,e). Zircon, monazite, and rutile are common accessory phases in metamorphic rocks. The BSE image shows a high concentration of halite in the majority of samples (MA-3 and M4). Its morphology is euhedral to subhedral cubic, but it occurs in a number of different sizes, growing between aggregates of micas or covering vast surfaces as agglomerated cubic crystals on the rest of the mineral surfaces, affecting the constituents of the fault-gouge material (Figures 6a,b and 7a–d). K- and Na-dioctahedral micas occur as thin, aggregated, foliated particles. (Figures 6c and 7a,b). A cataclasite texture is also observed, characterised by the presence of mineral and rock fragments that have undergone compaction and exhibit minimal porosity (Figure 6e,f).

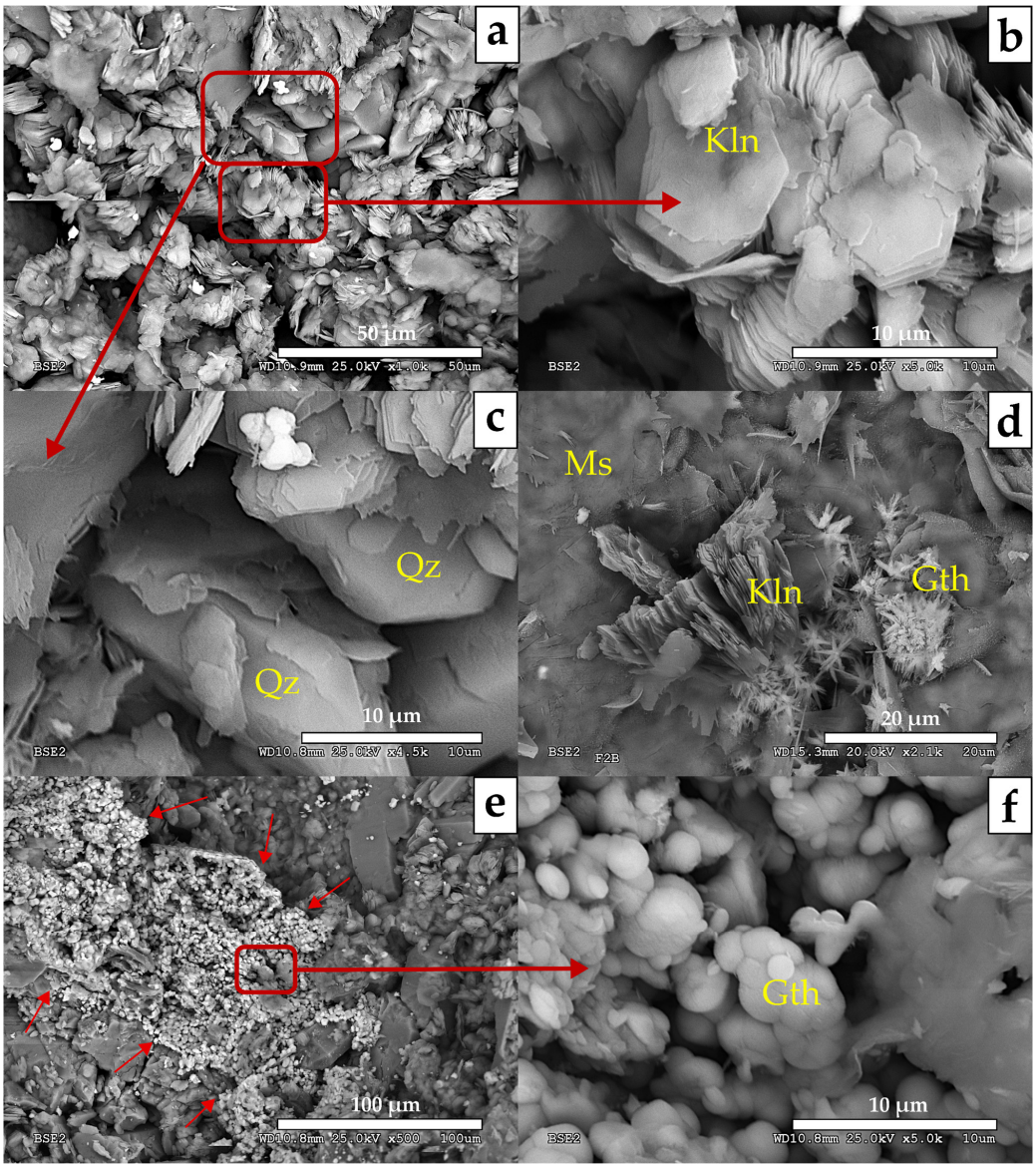

Figure 5. Mineral Assemblage 2 (MA-2). (**a**) Kaolinite aggregates forming book-like structures and euhedral quartz crystals (BSE); (**b**) Detail of kaolinite booklets (Kln) composed of stacked euhedral clay mineral crystals with grain sizes below 10 µm (BSE); (**c**) Detail of euhedral quartz crystals (Qz) enclosed within kaolinite aggregates, showing evidence of overgrowth (BSE); (**d**). Kaolinite booklets (Kln) and acicular radial aggregates of goethite (Gth) overgrowing muscovite (Ms) grain surfaces (BSE); (**e**) Granular coating of goethite (arrows) affecting material with a clastic texture (BSE); (**f**) A detailed view of the spheroidal morphology with a botryoidal appearance, which corresponds to goethite (Gth) (BSE).

Optical microscopy reveals a progressive textural variation in samples along the fault zone. MA-1 (metamorphic reference sample) shows a well-developed crenulation cleavage and a folded lepidoblastic texture (Figure 8a) composed of muscovite and quartz. Tourmaline, commonly reported in the Nevado-Filábride schists [77], is also present in this fault segment. Towards the fault core, the rock preserves its original texture, with slight development of cataclastic features and containing microfractures filled with iron oxides. One sample of the MA-2 exhibits attenuated crenulation, with microfolds flattened until foliation surfaces become parallel. Fine-grained metamorphic rocks, ranging from phyllite to microschist, display a foliated texture defined by muscovite mica sheets. Several microfractures also crosscut these rocks, some of them filled with hematite. Under crossed polars, a

grano-lepidoblastic texture highlights mica alignment and hematite within microfractures (Figure 8b,c). In MA-3, cataclastic textures become increasingly evident, characterized by grains of variable size and shape embedded in a darker matrix (Figure 8d). Metamorphic fragments are intersected by microcracks filled with hematite, suggesting also brittle deformation overprinted earlier metamorphic fabrics (Figure 8c). MA-4 displays microstructures with an oriented arrangement of stretched components, imparting a mylonitic aspect. Rock and mineral fragments occur within a matrix showing deformed lamination (Figure 8e). Quartz grains and micaceous aggregates of muscovite (Ms) are common (Figure 8f). Subhedral hematite grains are present within the oriented matrix, while dark cement locally disrupts metamorphic fragments, producing a chaotic appearance (Figure 9a,b). Finally, samples from MA-5, located near Neogene sediments, exhibit sedimentary textures. Sandy marl with a massive structure contains accumulations of bioclasts. Detailed views reveal foraminifera, some with dark infillings, along with dispersed quartz grains, indicating a mixed siliciclastic-carbonate composition (Figure 9c,d).

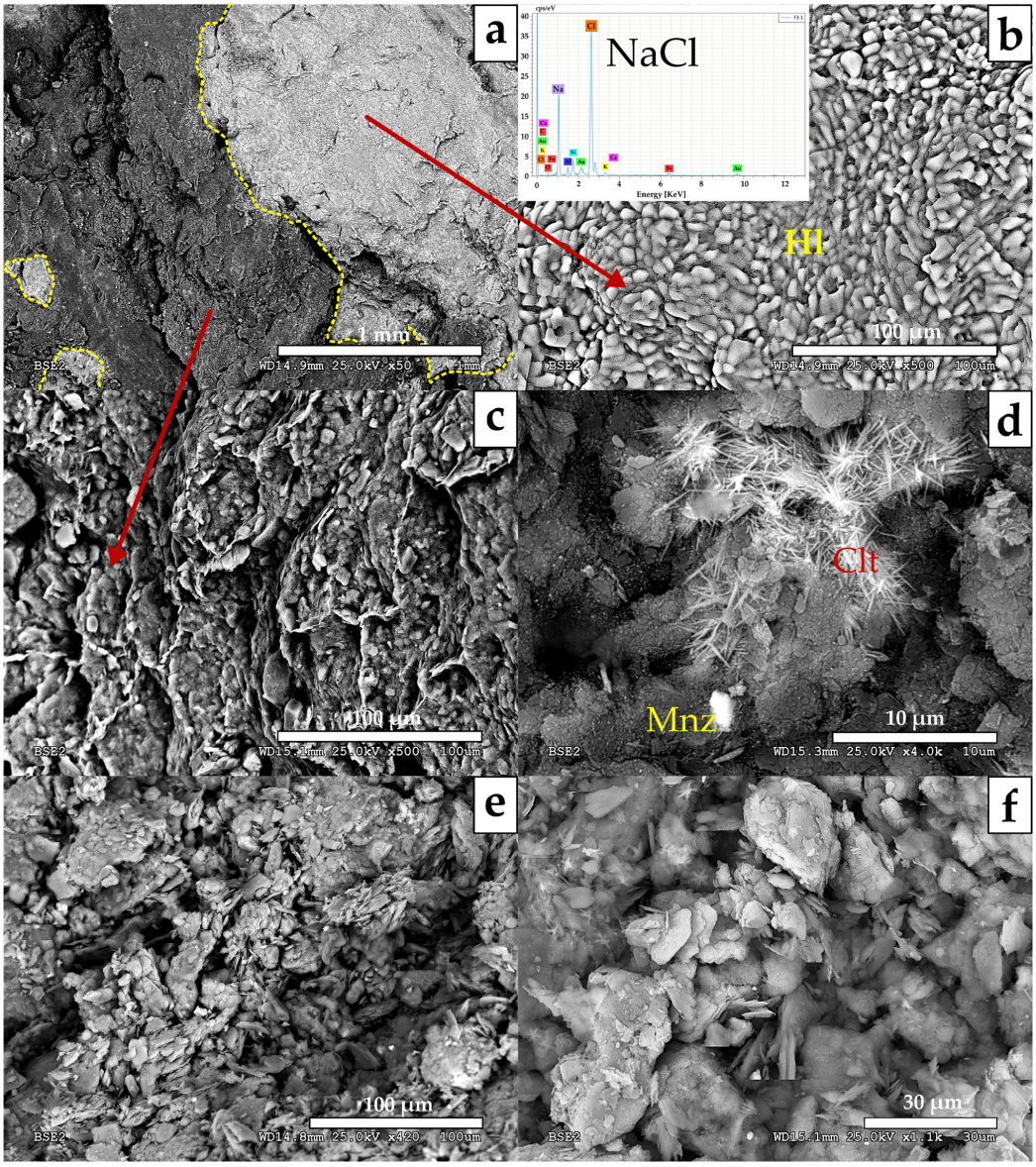

Figure 6. Mineral Assemblage 3 (MA-3). (**a**) Halite crusts coating fault gouge forming minerals surfaces (BSE). Halite crusts are marked with a yellow dotted line; (**b**) A detailed view of a halite (Hl)

crust composed of fine-grained, anhedral crystals cemented together (BSE). Inset: EDS spectrum indicates a high NaCl content; (**c**). Detail image of fault gouge material, illustrating a weak foliation that is characterised by the alignment of micaceous, platy grains(BSE); (**d**) Acicular celestine (Clt) crystals coating fault gouge surfaces and associated with diverse mineral grains, including monazite (Mnz) (BSE); (**e**) Chaotic, cataclastic texture with mixed mineral grains, some of them platy (BSE); (**f**) Section displaying a cataclastic texture, marked by compacted mineral and rock fragments with very low porosity (BSE).

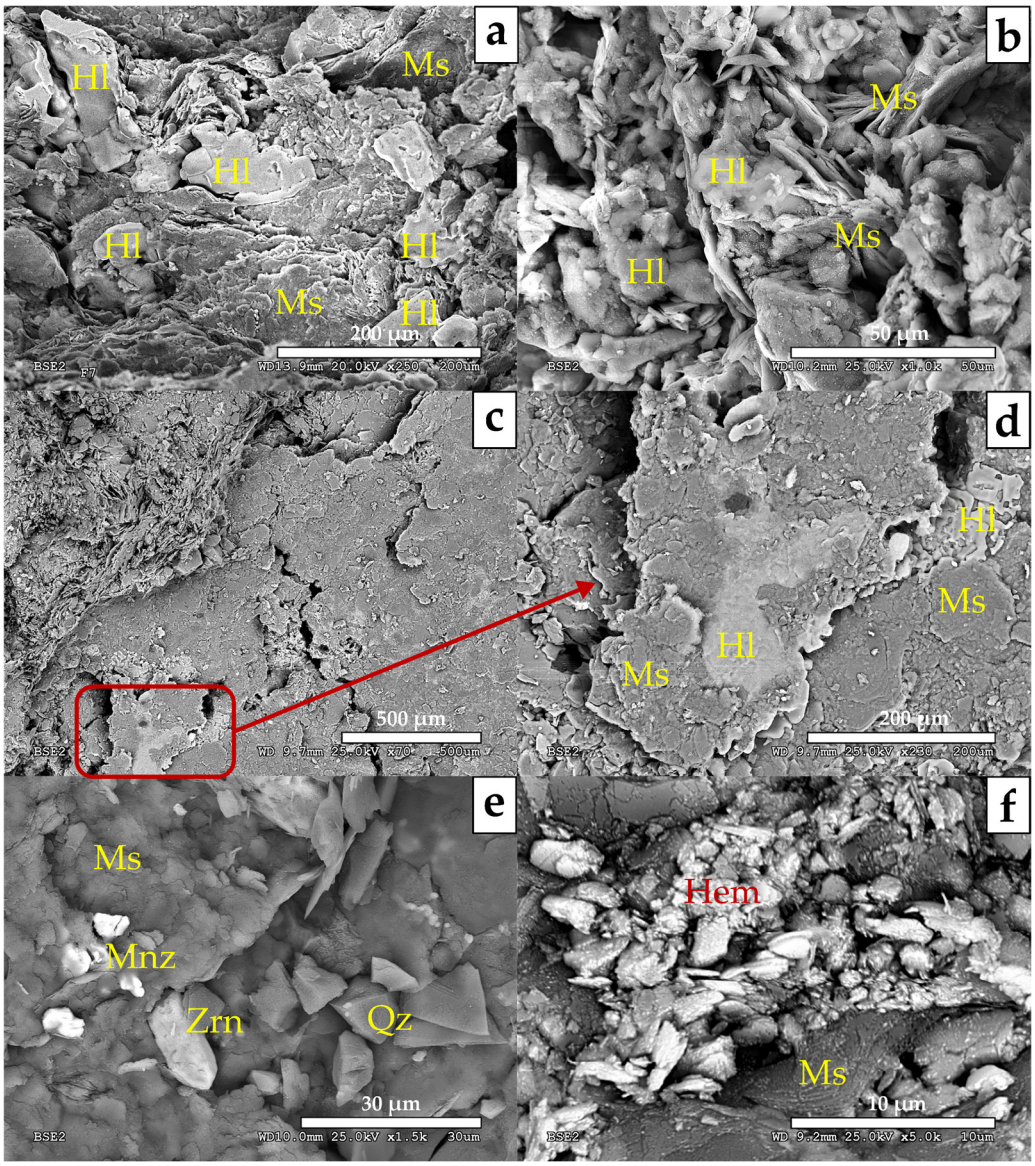

Figure 7. Mineral Assemblage 4 (MA-4). (**a**) Laminar microfabric characterized by mica grains (Ms) and halite (Hl). Anhedral halite crystals exhibiting dissolution features (BSE); (**b**) Detail of halite (Hl) crystals infilling pore spaces between muscovite (Ms) flakes (BSE); (**c**) General view showing variable orientations of sample constituents, emphasizing the abundance of micaceous, platy grains (BSE); (**d**) On planar surfaces, commonly defined by muscovite (Ms), halite crystals with dissolution features occur interlayered with mica sheets (BSE); (**e**) Dispersed within the fault gouge material, angular quartz grains (Qz), euhedral zircon (Zrn), and anhedral monazite grains (Mnz) have been identified (BSE); (**f**) Locally, hematite (Hem) grains have been identified, apparently infilling pore spaces (BSE).

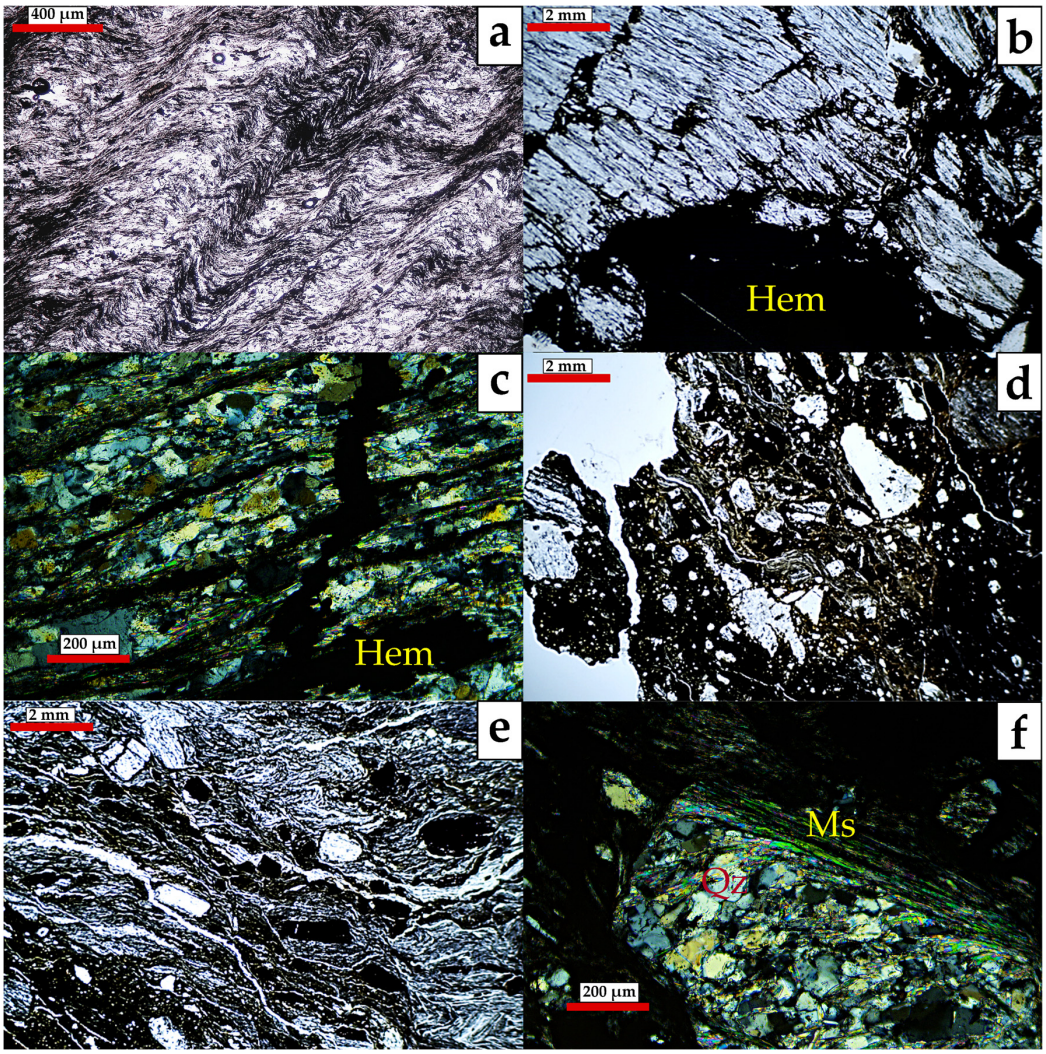

Figure 8. Mineral Assemblage 1 (MA-1): (**a**) Phyllite reference rock from the Nevado-Filábride Complex with well-developed crenulation cleavage and a folded lepidoblastic texture (Parallel nicols). **Mineral Assemblage 2 (MA-2):** (**b**) Foliated texture in fine-grained metamorphic rock (phyllite to microschist) affected by microfractures, some filled with hematite (Hem) (Parallel nicols); (**c**) Detail of the grano-lepidoblastic texture where muscovite micas define the foliation. A fracture filled with hematite cuts across the rock texture (Crossed nicols). **Mineral Assemblage 3 (MA-3):** (**d**) Cataclastic texture with grains of varying shapes and sizes embedded in a darker matrix (Parallel nicols). **Mineral Assemblage 4 (MA-4):** (**e**) Texture with oriented and stretched components giving a mylonitic appearance, where rock and mineral fragments are embedded in a matrix showing a slightly deformed lamination (Parallel nicols); (**f**) Detail of one fragment of metamorphic rock, where quartz grains (Qz) and micaceous aggregates of muscovite (Ms) can be identified (Crossed nicols).

5.2. Geochemistry

Geochemical trace element results were divided into different groups according to geochemical character and/or behaviour. In order to describe their variations along the fault segment, a series of geochemical profiles was compiled for LILE and lithium, HFSE, rare earth elements (REE), TTE, and chalcophiles, which are presented in Figure 10. Furthermore, graphs were produced considering the mobility of these elements along the fault zone. It was decided that certain elements from the chalcophile group (Ag, Cd, In, Se, Te) would be excluded from further consideration due to their concentrations below the detection limit (D.L). All element concentrations were normalised to their average abundance in

the Earth's continental crust from Rudnick and Gao [78]. The complete raw geochemical database can be found in Table 3.

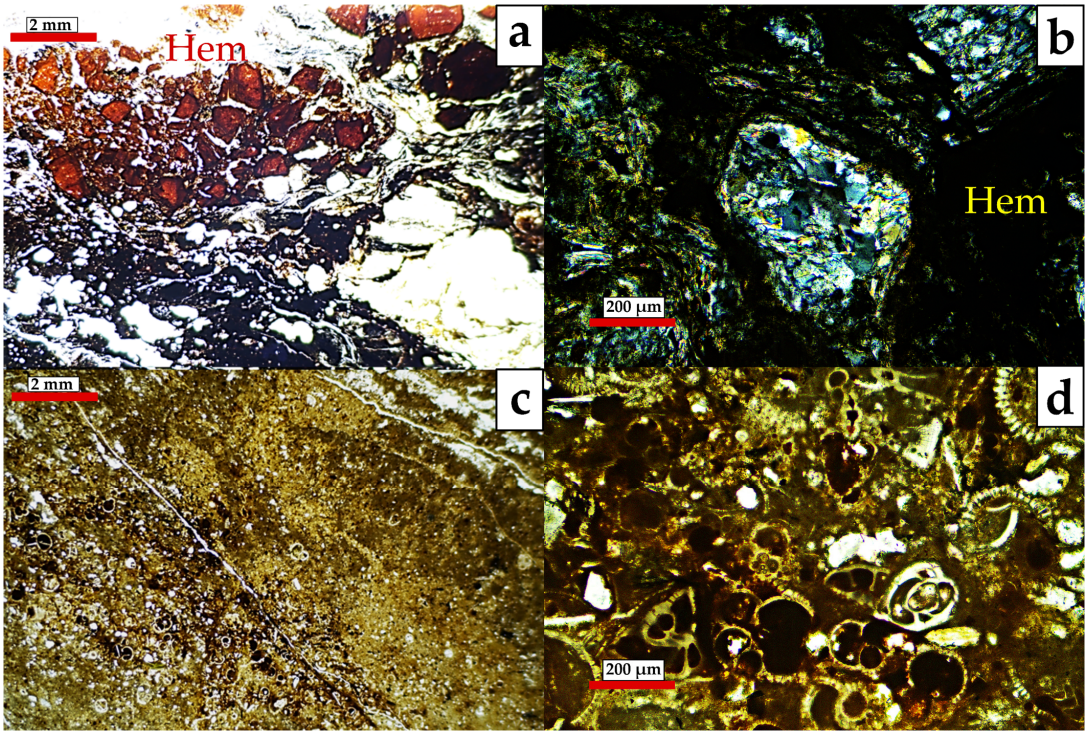

Figure 9. Mineral Assemblage 4 (MA-4): (**a**) Subhedral hematite (Hem) grains embedded in an oriented and deformed matrix containing grains of various sizes (Parallel nicols); (**b**) Section of metamorphic rock fragments, which appear to exhibit a chaotic appearance due to the presence of dark cement (Crossed nicols). **Mineral Assemblage 5 (MA-5):** (**c**) Sandy marl with a massive appearance, showing accumulations of bioclasts in a micritic matrix (Parallel nicols); (**d**) Detailed view of foraminifera bioclasts, some of which display dark infillings, as well as dispersed quartz grains (Crossed nicols).

There is a general enrichment of certain strategic elements in the fault core samples compared to the reference rock samples. The concentrations of Li (F7: 84 ppm), Rb (F7: 291 ppm), and K (F8: 3.91%) are higher than the average for continental crust (Figure 10a and Table 3). Ba and Sr, however, display concentrations either similar to or lower than those of the continental crust, with isolated anomalies in samples F10 (Ba: 3460 ppm; Sr: 2030 ppm) and F11 (Ba: 1350 ppm; Sr: 660 ppm) (sedimentary rock fault gouges), as well as, F4 (Ba: 1790 ppm; Sr: 170 ppm) which contains detectable barite in XRD (Table 2). Interestingly, Cs shows the strongest anomaly, reaching values up to ten times higher than those of average continental crust [78] across the entire fault core zone (F7: 98.8 ppm).

HFSE (Nb, Ta, Th, U, Ti), which are generally immobile and useful as environmental indicators, show values comparable to average continental crust abundances along the fault sequence (Figure 10b). Just like the REE pattern, the HFSE diagram for sample F2A presents a characteristic depletion in all HFSE, a feature also observed in the Neogene reference sample (F12), particularly in U (1.5 ppm) and Th (5.3 ppm).

The REE concentrations are broadly similar to those of average continental crust, with slight enrichment in the fault core samples (1.5–2 times the average continental crust abundances, Figure 10c). This is particularly evident in sample F7, which exhibits an anomaly in Eu, Tm, and Y, among others. Samples F2A and F2B, which are very close to metamorphic rock reference sample F1, exhibit different patterns of REE depletion: F2A

exhibits a negative anomaly in the HREE with no Eu anomaly, whereas F2B is depleted in the LREE.

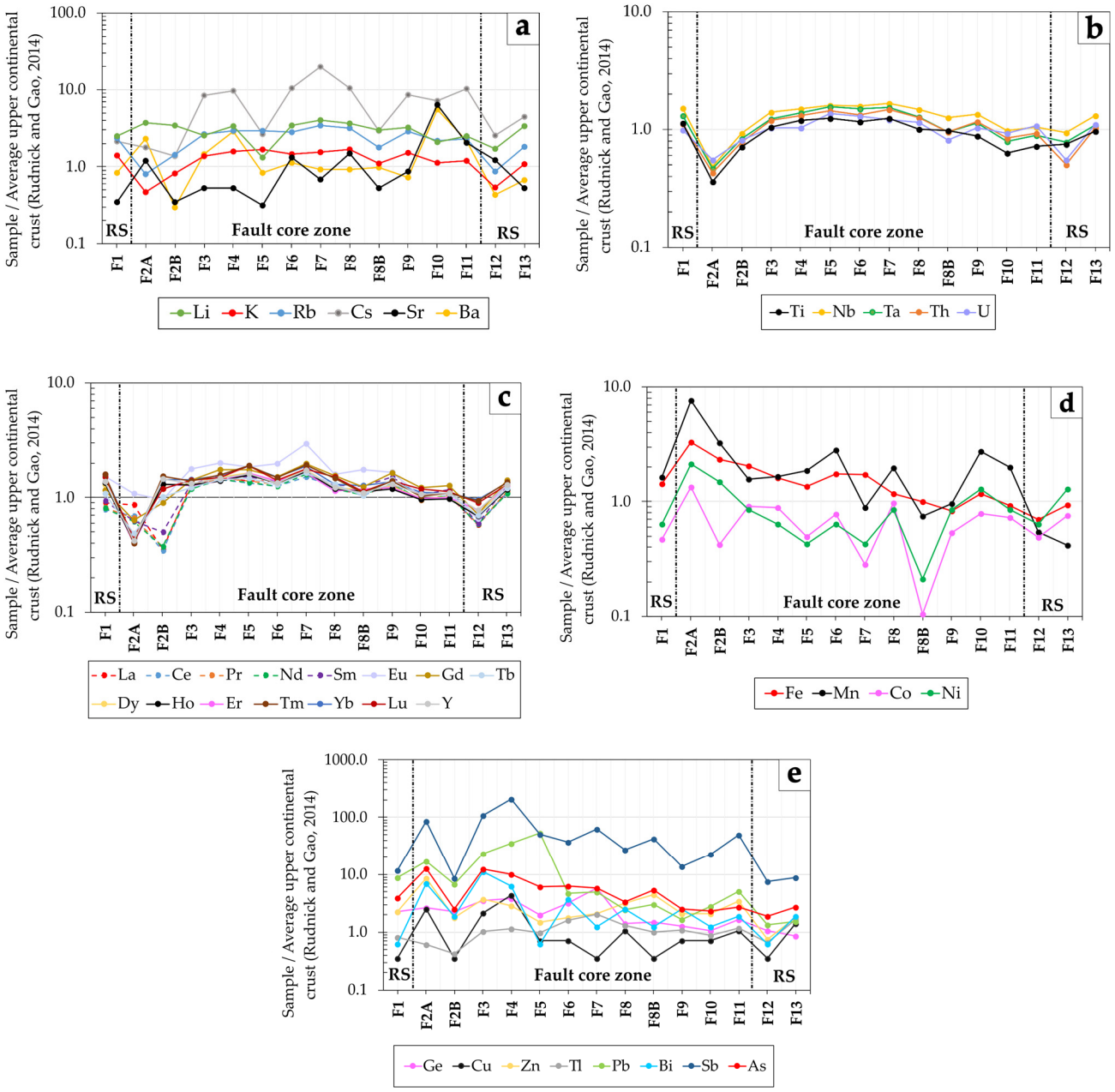

Figure 10. Geochemical profiles normalized to the average upper continental crust concentrations as established by Rudnick and Gao [78]. In the figures, the fault core zone and the reference samples (RS) are indicated. (**a**) LILE and Lithium profile; (**b**) HFSE profile; (**c**) REE profile; (**d**) TTE profile; (**e**) Chalcophile elements profile.

TTE geochemical profiles (Figure 10d) show that Co and Ni present a similar pattern, with a positive peak in sample F2A (Co: 23.2 ppm and Ni: 100 ppm) and a negative peak in F8B (Co: 1.8 ppm and Ni: 10 ppm). On average, their concentrations approximate those observed in average continental crust. Mn shows greater variability in concentrations along the fault segment, with general enrichment and a pronounced peak in F2A (5850 ppm), reaching nearly ten times the continental crust values. Fe also shows a clear trend with an increase in sample F2A (12.9%), followed by a slight decrease in the remaining samples.

Table 3. Geochemical database of samples from the El Arteal sinistral-normal fault.

		F1	F2A	F2B	F3	F4	F5	F6	F7	F8	F8B	F9	F10	F11	F12	F13
Li	ppm	53	79	73	54	71	28	73	84	77	63	68	44	53	36	71
Be	ppm	2.8	1.4	1.6	3.4	3.6	3.4	4.4	4.8	4	2.2	3.6	3.2	3.2	1.1	2.2
Mg	%	0.15	0.08	0.13	0.27	0.32	0.25	0.29	0.45	1.1	0.17	0.99	0.96	1.12	1.18	1.76
Ca	%	0.1	0.1	0.1	0.1	0.2	0.1	0.1	0.2	1	0.2	7.1	14.6	10	3.2	2.3
K	%	3.23	1.09	1.91	3.21	3.67	3.88	3.41	3.62	3.91	2.58	3.5	2.62	2.8	1.26	2.49
Rb	ppm	198.5	67.3	120	223	249	245	235	291	265	149.5	242	181.5	193.5	72.3	153.5
Cs	ppm	10.4	8.7	6.8	41.6	48	13	51.8	98.8	52	14.5	42.5	35	50.2	12.6	21.9
Sr	ppm	110	380	110	170	170	100	420	220	480	170	280	2030	660	390	170
Ba	ppm	517	1450	185	918	1790	518	703	578	575	610	455	3460	1350	271	419
Ti	%	0.538	0.172	0.336	0.499	0.571	0.593	0.555	0.59	0.476	0.462	0.416	0.301	0.343	0.358	0.458
Nb	ppm	18.3	5.8	11.2	16.8	18	19.3	19.1	20	17.8	15.2	16.2	11.8	12.6	11.3	15.8
Ta	ppm	1.18	0.42	0.75	1.11	1.24	1.4	1.36	1.38	1.16	0.86	1.02	0.71	0.8	0.7	0.98
Th	ppm	11.8	4.5	8.2	12.6	13.9	15.2	14	15.6	13.2	10	12.3	8.9	9.8	5.3	10.8
U	ppm	2.7	1.5	2.2	2.8	2.8	3.7	3.5	3.3	3.1	2.2	2.8	2.5	2.9	1.5	3
La	ppm	27.7	26.6	11	40	46.3	43.5	43.3	51.6	37.3	32.8	39.8	29.9	32.2	17.9	34.5
Ce	ppm	49.4	43.5	21.8	74.5	90.4	84.1	79.1	95.3	79.5	65.5	82.8	60.4	65.5	37.4	68.5
Pr	ppm	5.84	4.67	2.65	8.79	10.45	9.89	9.23	11.4	8.53	7.8	9.2	6.77	7.5	4.16	7.97
Nd	ppm	21.9	16.75	10.05	31.9	38.7	36.9	33.9	42.8	32	28.3	35.9	25.9	28	15.85	29.4
Sm	ppm	4.41	2.95	2.35	6.14	7.32	7.07	6.52	7.9	6.04	5.89	7.07	4.98	5.52	2.78	5.99
Eu	ppm	1.53	1.08	0.96	1.77	2	1.85	1.98	2.95	1.6	1.76	1.67	1.03	1.1	0.65	1.31
Gd	ppm	4.61	2.53	3.59	5.69	7.02	6.99	6.08	7.9	6.17	4.97	6.55	4.9	5.07	2.88	5.63
Tb	ppm	0.76	0.34	0.71	0.86	1	1.03	0.9	1.14	0.91	0.73	1	0.73	0.76	0.49	0.84
Dy	ppm	5.05	1.83	5.01	5.09	5.91	6.37	5.47	6.86	4.79	4.57	4.89	3.85	3.96	2.76	4.96
Ho	ppm	1.12	0.34	1.08	1.07	1.16	1.31	1.11	1.4	0.99	0.93	0.99	0.8	0.81	0.57	0.97
Er	ppm	3.17	0.91	2.99	2.92	3.21	3.79	3.21	3.78	2.64	2.73	2.79	2.26	2.31	1.78	2.87
Tm	ppm	0.48	0.12	0.46	0.42	0.47	0.57	0.45	0.58	0.44	0.33	0.42	0.31	0.33	0.28	0.41
Yb	ppm	3.16	0.87	2.86	2.85	3.09	3.75	3.01	3.76	2.62	2.53	2.75	2.21	2.18	1.92	2.68
Lu	ppm	0.47	0.14	0.37	0.44	0.46	0.59	0.44	0.55	0.47	0.35	0.43	0.37	0.35	0.28	0.4
Y	ppm	28.9	8.8	30.4	27.8	30.8	34.1	28.3	36.5	25.5	23.1	27.3	22.5	23.1	16.2	27.1
Fe	%	5.57	12.9	9.15	8.05	6.28	5.32	6.83	6.75	4.61	3.93	3.26	4.61	3.6	2.73	3.67
Mn	ppm	1260	5850	2530	1220	1280	1440	2190	690	1520	580	740	2130	1550	420	320
V	ppm	131	51	79	144	152	163	166	182	138	96	123	90	100	61	113
Co	ppm	8.1	23.2	7.3	15.8	15.4	8.6	13.4	4.9	16.8	1.8	9.3	13.6	12.6	8.4	13
Ni	ppm	30	100	70	40	30	20	30	20	40	10	40	60	40	30	60
Mo	ppm	2	3	2	2	2	2	2	3	2	<2	<2	<2	<2	<2	<2
W	ppm	8.4	5.6	10.4	9.6	11	6.7	12.2	32.3	6.3	13.1	4.3	3	2.5	1.6	2.5
Re	ppm	<0.01	<0.01	<0.01	<0.01	0.01	<0.01	<0.01	0.01	0.03	<0.01	0.03	0.02	0.02	0.01	<0.01
Ga	ppm	24.3	9	14.2	24.4	26.9	29.2	29.3	31.3	26.2	18.9	24.2	16.8	19.3	10.9	20.5
Ge	ppm	3.2	3.7	3.2	4.9	5.3	2.8	4.5	6.4	2	2.1	1.8	1.5	2.3	1.5	1.2
Cu	ppm	<20	70	<20	60	120	20	20	<20	30	<20	20	20	30	<20	40
Zn	ppm	150	570	120	250	190	100	120	140	210	300	140	140	230	50	40
Ag	ppm	<5	<5	<5	6	7	<5	<5	<5	<5	<5	<5	<5	<5	<5	120
Cd	ppm	<0.8	1	<0.8	<0.8	<0.8	<0.8	<0.8	<0.8	<0.8	1.4	<0.8	<0.8	<0.8	<0.8	<0.8
In	ppm	<0.3	0.3	<0.3	<0.3	<0.3	<0.3	<0.3	<0.3	<0.3	<0.3	<0.3	<0.3	<0.3	<0.3	<0.3
Sn	ppm	15	9	13	15	19	18	16	13	7	13	5	5	4	4	<3
Tl	ppm	0.82	0.61	0.42	1.02	1.16	0.99	1.6	2.01	1.32	1	1.09	0.88	1.17	0.67	1.66
Pb	ppm	149.5	287	114	392	594	900	80.1	83.2	41.4	50.6	28.3	46.9	86.3	22.5	26.2
Bi	ppm	0.1	1.1	0.3	1.8	1	0.1	0.6	0.2	0.4	0.2	0.4	0.2	0.3	0.1	0.3
Sb	ppm	4.7	34.3	3.4	43.3	82.5	20	14.7	24.8	10.9	16.7	5.5	8.9	19.8	3	3.5
As	ppm	19	61	12	60	48	29	30	28	16	26	12	11	13	9	13
Te	ppm	<0.5	<0.5	<0.5	<0.5	<0.5	<0.5	<0.5	<0.5	<0.5	<0.5	<0.5	<0.5	<0.5	<0.5	<0.5
Se	ppm	<3	<3	<3	3	<3	<3	4	<3	<3	<3	<3	<3	<3	3	<3

Chalcophile elements display a distinct trend across the fault zone (Figure 10e). In samples collected near the metamorphic reference rocks (uplifted block) from F2A to F6, As, Sb, Bi, Cu, Pb, and Zn show significant enrichment, with anomalies ranging from seven (As, Bi, Cu, Zn) to one hundred times (Sb, 82.5 ppm in F4 and Pb, 900 ppm in F5), the

average continental crust abundances. An exception is sample F2B, which records lower concentrations comparable to those of the reference sample (F1). Toward the center of the fault from F5 to F9, the geochemical patterns become more variable. Sb remains highly anomalous throughout the fault gouge samples, while its concentrations decrease in the Nevado-Filábride Complex and Neogene sediments reference samples. In contrast, As, Pb, and Bi display slight decreases from F3–F5 onwards, while Cu is depleted relative to crustal values. The concentrations of Tl and Ge are found to be in close proximity to those observed in the continental crust. However, a marginal increase is noted in samples obtained from the fault core (F7, with 6.4 ppm Ge and 2 ppm Tl; Table 3).

5.3. Element Associations

A statistical method was implemented using RStudio version 2025.09.0+387 and the R software version 4.5.1 for statistical computing and graphics. The Pearson correlation matrix is a statistical tool used to analyse the relationships among the geochemical elements under investigation (see Figure 11) and it was created with 42 variables, or elemental concentrations: Li, Be, Mg, Ca, K, Rb, Cs, Sr, Ba, Ti, Nb, Ta, Th, U, La, Ce, Pr, Nd, Sm, Eu, Gd, Tb, Dy, Ho, Er, Tm, Yb, Lu, Y, Fe, Mn, V, Co, Ni, Cu, Zn, Sn, Tl, Pb, Bi, Sb, As. Variables with more than 50% of concentrations below the detection limit (D.L.) were excluded from the statistical analysis. For Cu and Sn, with less than 50% of their concentrations below the detection limit, it was chosen to fill these gaps with half the detection limit values, but taking into account that their results are subject to a large error and should be interpreted with caution. W, Ga, and Ge were not considered in the Pearson correlation matrix.

The Pearson correlation matrix reveals coherent associations among element groups that help distinguish immobile vs. mobile behaviour and mineralogical controls (see Figure 11). A well-defined pattern of moderately strong to very strong positive correlations (coefficients from 0.60 to 0.96, close to 1) is observed among the REE, although the higher ones correlate elements belonging to the same subgroup (e.g., 0.98 (La-Nd, both LREE) or 0.99 (Yb-Er, both HREE)) and the lower ones correlate light versus heavy REE (E.G., 0.55 La-Yb or 0.63 Nd-Er). HREE, in addition, tend to show high correlation coefficients with HFSE, e.g., 0.90 (Nb-Yb) or 0.90 (Ti-Yb), which could indicate a similar geochemical behaviour.

Interestingly, all REE exhibit significant positive correlations with certain LILE (K, Rb, Cs), as evidenced by the following coefficients: 0.88 (Rb-Nd), 0.72 (Cs-La), 0.94 (Rb-Gd), or 0.79 (K-Yb). However, for Li, Ba, and Sr, these correlations are non-existent, for instance LREE-LILE:0.08 (La-Ba), −0.12 (La-Sr), and 0.20 (La-Li), and HREE-LILE: −0.32 (Yb-Ba), −0.34 (Yb-Sr), and −0.05 (Yb-Li). Li is decoupled from almost all the rest of LILE except Cs, with which it shows a poor correlation coefficient of 0.43.

Further, positive correlation coefficients ranging from 0.70 to 0.89 have been observed among certain chalcophile elements, particularly As, Sb, Bi, and Cu. In turn, several transition elements (TTE), including those forming oxide minerals: Co, Ni, Fe, and Mn, exhibit positive correlations with one another (0.50–0.83). However, correlations between elements from each group (chalcophile and TTE) are variable. For example, Fe shows a nice positive correlation with As (0.71, the highest coefficient among the chalcophile elements), and the latter, in turn, correlates moderately well with Co 0.52 (As-Co) and Mn 0.48 (As-Mn). However, Sb shows only a very poor correlation coefficient with Fe: 0.36 (Fe-Sb) and a similar one with Co: 0.39 (Sb-Co). Moreover, the correlations between oxide minerals and LILE are not significant, e.g., 0.42 (Fe-Li) or −0.14 (Co-K).

In summary, three element associations can be outlined: (1) high correlation HFSE with HREE, (2) some LILE (K, Rb, Cs) with REE; (3) As (chalcophile elements) with TTE

(Fe, Mn, Co), plus a fourth one involving Ca, Sr, and Ba, with notable correlations between them, 0.85 (Sr-Ba) and 0.84 (Sr-Ca), 0.66 (Ca-Ba).

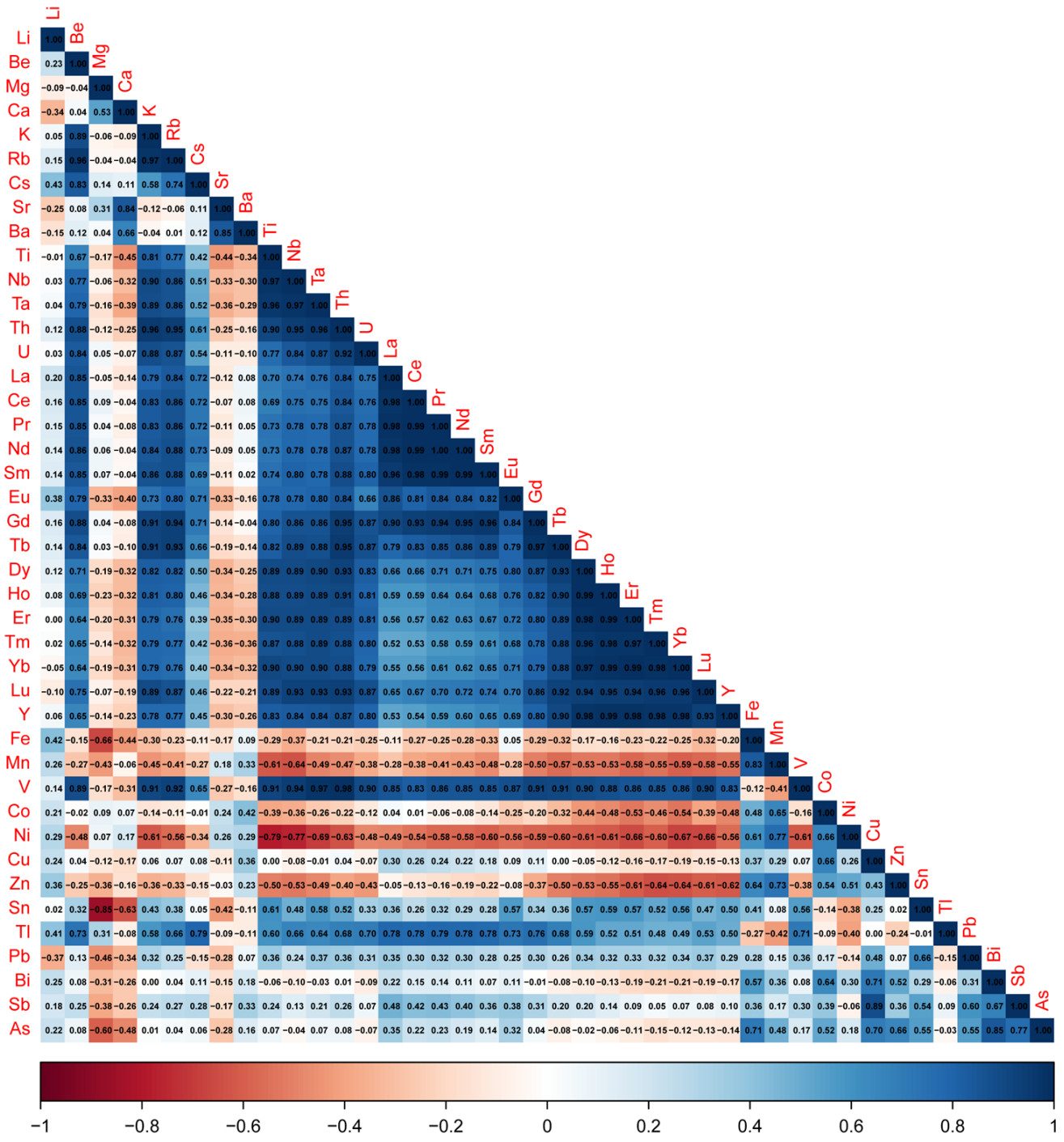

Figure 11. Pearson correlation matrix of 42 elements concentrations, where correlation coefficients are shown in a graphical way, such that small size and light colours symbols indicate poor or no correlation, and large symbols and dark colour indicate close to 1 (positive, blue) or close to −1 (negative, red) values.

5.4. Hydrochemical Data

Chemical analyses in the seven water samples show two types of facies in the Stiff diagrams (Figure 12 and Table 4). The well located in quaternary sediments (ART-1) presents sodium-sulphate facies with the highest NO_3^- contents. The remaining water samples ex-

hibit a sodium–chloride hydrochemical facies. However, the relative concentrations of Na^+, Cl^-, Mg^{2+}, NO_3^-, and SO_4^{2-} vary significantly, allowing the distinction of three discrete Na–Cl subfacies within the dataset (Figure 12). In Table 4, from well ART-2 (in the vicinity of the fault zone) to the experimental deep well (S.A.), sodium and chloride concentrations increase progressively with both temperature and depth. Conversely, sulphate (SO_4^{2-}) and silica (Si) contents show a marked decrease, correlating with the sharp rise in Na^+ and Cl^- levels at greater depths and higher temperatures. Chloride concentrations intensify notably toward the deeper and more internal sectors of the Almagrera Range. Na^+, K^+, Ca^{2+}, and Mg^{2+} content in Table 4 also suggests that these elements are enriched at greater depths and higher temperatures. Conversely, these elements do not increase to the same extent as chloride, suggesting a partial ionic imbalance between major cations and anions. Among the trace elements, LILE (Li, Ba, Sr) and B concentrations increase toward the interior of the Almagrera Range, also associated with greater depth, higher chloride content, and elevated temperatures. A similar trend is observed for Rb and Cs in wells located at the El Arteal mine dewatering system. In contrast, rare earth element concentrations are generally low and not significant in any of the water samples. The Cl/Br ratio further distinguishes two hydrochemical facies: one associated with the shallow wells (ART-1 and ART-2) and another with the deeper ones (ART-3, ART-4, and S.A.). According to Alcala and Custodio [71] and historical data in Section 3, Cl/Br ratios in ART-3, ART-4, and S.A. exceed those of seawater, while farming activity may influence ART-1 and ART-2. It has been observed that pH tends to decrease slightly in the Almagrera Range area and at depth. Nevertheless, that pH trend is exhibited more distinctly in the historical data (Guzmana mine shaft, see Table 1). The remaining trace elements obtained (Table 4) demonstrate an absence of notable REE presence in groundwater. HFSE data, as expected, do not reveal any anomalies in content. However, a slight decline in uranium has been observed in mine shafts in proximity to the metamorphic rocks.

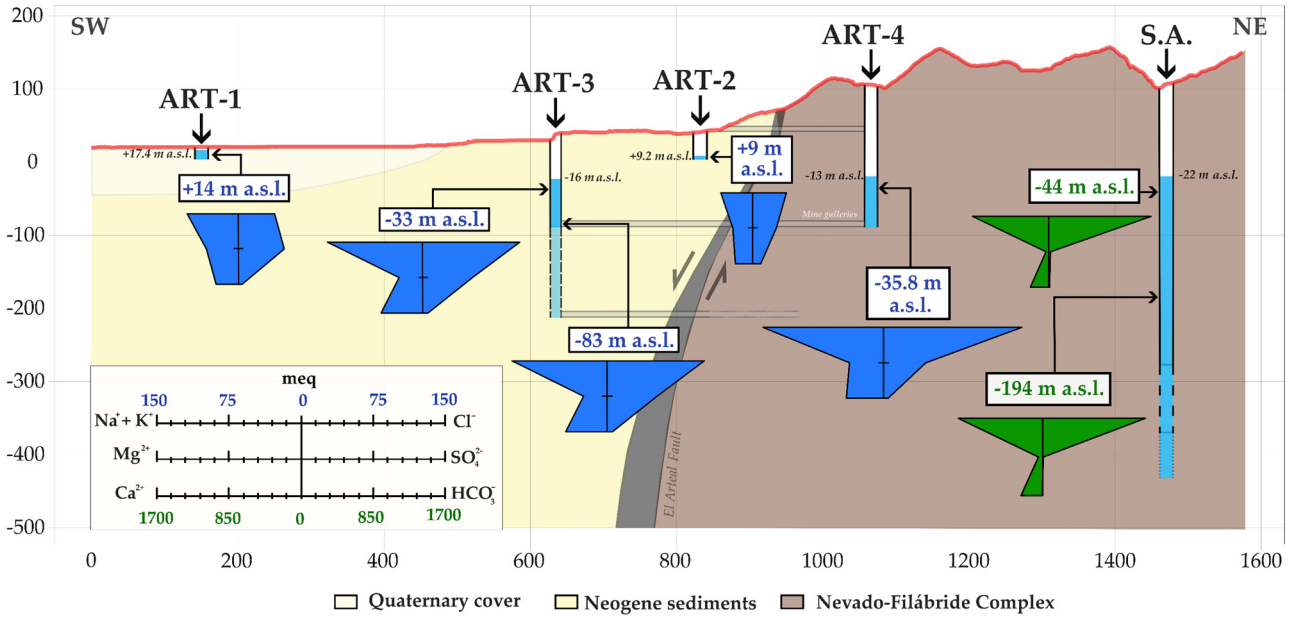

Figure 12. Stiff diagrams of the water samples taken. Scale is expressed in milliequivalents (meq): The upper numbers in blue colour correspond to the scale of the blue Stiff diagrams, while the green numbers positioned at the bottom indicate the scale of the green Stiff diagrams. ART-1 and ART-2: Wells for water supply; ART-3 and ART-4: El Arteal mine dewatering; and S.A: Experimental Deep Well. Figures in italics show the piezometric head metres above sea level (m a.s.l.) and figures in the white rectangles represent the sampling depth in m above sea level. Both axes are in metre units.

Table 4. Major ions and trace elements of the seven samples surrounding the El Arteal fault. Dash (-) is no data.

Parameters	ART-1	ART-2	ART-3	ART-3-120	ART-4	S.A.-150	S.A.-300
Well depth (m)	12.4	33.1	122.5 [1]	122.5 [1]	192.5	550	550
Well depth (m a.s.l.)	8	8	−86	−86	−86	−86	−444
Piezometric head (m a.s.l.)	17.4	9.2	−16.7	−16	−13	−22	−22
Sampling depth (m a.s.l.)	14	9	−33	−83	−35.8	−44	−194
T (°C)	22.3	22.9	32	ND	34.5	34	42.7
pH	6.02	7.16	7.24	7.13	6.73	7.26	5.64
Conductivity (µS/cm)	9018	6261	13,400	9980	16,600	121,498	138,126
TDS (mg/L)	5970	4550	9780	9870	12,800	96,900	99,100
Na (mg/L)	1230	750	2230	2170	2830	20,600	20,600
Ca (mg/L)	479	362	871	895	779	5160	5140
K (mg/L)	48.5	38.6	147	151.5	193	1380	1415
Mg (mg/L)	416	253	296	298	431	542	543
Cl (mg/L)	1360	1290	3700	3340	5280	43,600	40,600
SO_4 (mg/L)	2340	1230	2590	2000	2220	600	573
HCO_3 (mg/L)	237	550	398	448	359	33	1.22
NO_3 (mg/L)	46.7	0.341	<0.5	<0.5	<0.5	<5	<5
B (mg/L)	2.84	1.33	5.12	5.3	5.69	24	24
Ba (mg/L)	0.019	0.015	0.030	0.033	0.028	0.34	0.4
Br (mg/L)	3.9	2.6	<5	<5	5.8	40	36.9
Cs (mg/L)	0.001	0.003	0.221	0.246	0.529	-	-
F (mg/L)	<1	<1	<2	<2	<2	<10	<10
Fe (mg/L)	0.072	0.027	0.047	0.145	0.004	<0.5	4.3
Li (mg/L)	0.66	0.76	5.35	5.53	7.39	59.5	59.4
Mn (mg/L)	0.04	0.02	0.098	1.06	22	3.9	4.7
Rb (mg/L)	0.064	0.024	0.765	1.035	1.345	-	-
Si (mg/L)	11.4	11.3	15.5	13.6	10.6	0.1	0.1
Sr (mg/L)	13.4	7.2	21.4	21.9	18.9	185	186
Ag (µg/L)	0.831	0.219	<0.005	0.014	0.079	<10	<10
Al (µg/L)	12	7	4	19	<3	700	700
As (µg/L)	1.13	0.38	0.71	1.02	2.21	<100	<100
Be (µg/L)	0.006	0.032	<0.005	0.087	<0.005	<0.5	<0.5
Bi (µg/L)	0.02	0.05	<0.01	0.03	<0.01	-	-
Cd (µg/L)	0.055	0.059	0.009	0.034	8.15	<5	<5
Ce (µg/L)	<0.005	<0.005	0.062	0.015	0.013	-	-
Co (µg/L)	0.943	0.153	0.325	1.055	89.7	70	70
Cr (µg/L)	2	0.5	<0.5	1	<0.5	<0.5	<0.5
Cu (µg/L)	7.5	1.5	0.7	1.2	1.5	10	<10
Dy (µg/L)	<0.005	<0.005	<0.005	<0.005	<0.005	-	-
Er (µg/L)	<0.005	0.007	<0.005	0.005	<0.005	-	-
Eu (µg/L)	<0.005	<0.005	0.005	0.008	0.005	-	-
Ga (µg/L)	<0.05	<0.05	0.08	<0.05	0.06	-	-
Gd (µg/L)	0.01	<0.005	<0.005	<0.005	<0.005	-	-
Hf (µg/L)	<0.005	<0.005	0.008	0.015	0.008	-	-
Hg (µg/L)	<0.05	<0.05	0.13	<0.05	0.08	-	-
Ho (µg/L)	<0.005	<0.005	<0.005	<0.005	<0.005	-	-
La (µg/L)	0.007	0.018	0.005	0.016	<0.005	-	-
Lu (µg/L)	<0.005	<0.005	<0.005	<0.005	<0.005	-	-
Mo (µg/L)	1.11	0.95	1.99	2.22	0.59	-	-
Nb (µg/L)	0.007	0.007	<0.005	0.017	<0.005	-	-
Nd (µg/L)	0.012	0.007	<0.005	0.009	<0.005	-	-
Ni (µg/L)	13.6	3.2	7.9	4.6	260	100	100
P (µg/L)	96	107	757	762	<5	<500	<500
Pb (µg/L)	1.34	0.76	0.27	1.02	<0.05	<50	<50
Pd (µg/L)	0.103	0.015	0.103	0.033	0.043	-	-

Table 4. *Cont.*

Parameters	ART-1	ART-2	ART-3	ART-3-120	ART-4	S.A.-150	S.A.-300
Pt (µg/L)	0.006	0.005	0.006	<0.005	0.006	-	-
Pr (µg/L)	<0.005	<0.005	<0.005	<0.005	<0.005	-	-
Sb (µg/L)	4.4	0.32	0.55	0.05	0.66	<100	<100
Sc (µg/L)	1.89	1.38	0.43	0.77	<0.01	<50	<50
Se (µg/L)	12.4	7.9	0.14	<0.05	0.49	-	-
Sm (µg/L)	0.009	<0.005	<0.005	<0.005	<0.005	-	-
Sn (µg/L)	0.19	<0.05	<0.05	0.11	<0.05	-	-
Ta (µg/L)	<0.01	<0.01	<0.01	0.01	<0.01	-	-
Tb (µg/L)	<0.005	<0.005	<0.005	<0.005	<0.005	-	-
Te (µg/L)	0.02	0.02	0.02	0.07	<0.01	-	-
Th (µg/L)	0.011	<0.005	0.014	0.101	0.005	-	-
Ti (µg/L)	<0.2	<0.2	<0.2	<0.2	<0.2	<5	<5
Tl (µg/L)	0.091	3.2	0.13	0.047	48.4	-	-
Tm (µg/L)	<0.005	<0.005	<0.005	<0.005	<0.005	-	-
U (µg/L)	20.7	8.9	2.31	2.48	3.44	-	-
V (µg/L)	0.45	0.71	0.43	0.7	0.18	<10	<10
W (µg/L)	0.01	0.01	0.33	0.21	0.01	-	-
Yb (µg/L)	0.005	0.007	<0.005	<0.005	<0.005	-	-
Y (µg/L)	0.098	0.072	0.011	0.074	0.116	-	-
Zn (µg/L)	34.2	22.4	26.7	1.6	3660	<20	50
Zr (µg/L)	0.11	0.02	0.07	0.05	<0.02	-	-
Cl/Br	349	500	1480 [2]	1336 [2]	910	1090	1100
Rb/Cs	65.6	7.1	3.5	4.2	2.5	-	-
Ca/Cl	0.35	0.28	0.24	0.27	0.15	0.12	0.13
Mg/Cl	0.31	0.20	0.08	0.09	0.08	0.01	0.1
Na/Cl	0.90	0.58	0.60	0.65	0.54	0.47	0.51

[1] During mining operations, ART-3 was re-deepened to 250–257 m, currently collapsed at 122.5 m.
[2] Br below detection limit; half the D.L value assigned.

6. Discussion

The combined mineralogical, textural, geochemical, and hydrochemical results presented in this study provide new insights into the configuration and evolution of the geothermal Águilas Arc system.

6.1. Fault Rock Mineralogy: Implications for Hydrothermal (Re)Activation

Fault zones are defined as highly dynamic structural domains, where rocks undergo significant deformation, thereby profoundly modifying their mechanical behaviour, microstructures, and permeability architecture. The mylonitic texture (ductile shearing) and the cataclastic brecciation (brittle fracturing) observed under the optical microscope and SEM observations in the fault gouge samples show the result of Pliocene and Quaternary fault activity [37,38] (Figures 6e,f and 8d,e). These processes have been shown to increase the permeability of the Almagrera Range, thereby enhancing fluid circulation, particularly within the fault zones [16,17]. The thermal waters identified during the dewatering of the mine shafts are likely to reflect fluid-rock interaction processes. In particular, the presence of newly crystallized phyllosilicates and quartz in some samples from the fault gouge is worthy of note [79,80]. Evidence of this phenomenon can be seen in the XRD patterns, which shows a significant increase in the content of phyllosilicates, at the expense of feldspars, ranging from 25% in reference sample F1 (MA-1), to 40% in fault gouges F3 to F5 (MA-3), and up to 64% in samples F6 to F8B (MA-4) from the fault centre. In samples F9 to F11 (MA-5), which are close to the MA-6 reference samples, the percentage of phyllosilicate minerals drops again to 33% (see Table 2). There is also neoformation of clay minerals, with illite and kaolinite aggregates forming book-like structures (see Table 2 and

Figure 5a–c). New authigenic phases, including quartz, halite, goethite, hematite, barite, and celestine, have also developed in the fault gouge samples. Textural and morphological evidence indicate that the illite identified in the studied samples was formed under hydrothermal conditions rather than during burial diagenesis. Hydrothermal illite typically develops in high-porosity, fluid-dominated systems through dissolution of previous smectites and recrystallization in larger particle sizes with hexagonal rather than elongated morphologies [81].

The coexistence of illite and kaolinite in the studied samples indicates a hydrothermal alteration environment characterized by intermediate to advanced argillic facies. Kaolinite typically forms under acidic conditions (pH = 4.5–6) and relatively low temperatures (<200 °C), whereas illite is stable at higher temperatures (>200 °C) and near-neutral pH = 5.5–7, commonly associated with phyllic alteration zones [82]. This mineral assemblage suggests a progressive evolution of hydrothermal fluids, from moderately acidic and low-temperature conditions toward more neutral and hotter environments, reflecting dynamic water–rock interaction during fluid circulation. These physicochemical parameters favour the alteration of K-feldspar and other aluminosilicates, leading to the release of K^+, Al^{3+}, and silica into the circulating fluids. The liberated silica subsequently precipitates as authigenic and euhedral quartz within pores and fractures (in a late-stage), establishing a characteristic association between kaolinite, illite, and quartz in hydrothermal alteration zones [82–84]. Similar observations have been recently described in some other segments of the Palomares Fault Zone and nearby related faults, remarking the role of hydrothermal alteration and clay mineral neoformation in fault gouges [16,85,86], where illite, chlorite, and smectite are among the most common low-temperature alteration products [85]. In addition, as part of the characterization of geothermal systems, Sanjuan [2] has pointed out that the most common fluid-rock interaction processes at temperatures (≥120 °C), are dominated by: plagioclase and K-feldspar dissolution, followed by albitization of these minerals, dissolution of white micas and biotite, precipitation of illite, and chloritization, although the latter was not observed in our studied fault segment.

Paragonite, a sodium-rich white mica located from sample F5 to F13, serves as an indicator of fluid–rock interaction and metasomatic processes. Its formation in hydrothermal systems typically occurs via replacement of K-feldspar or muscovite in the presence of Na-rich fluids, or through recrystallization of aluminous phases under low to moderate temperatures and acidic conditions [87]. The presence of halite exclusively within the mineral assemblage (MA-2, MA-3, MA-4, and MA-5) of the fault zones in the Almagrera Range indicates the entrapment and circulation of highly saline fluids (brines) only in this pathway. This is associated with complex fluid-rock interaction processes in a geothermal system. This interpretation is supported by the hydrogeological data obtained in this study, which confirm the existence of chloride-rich deep brines in the region [36].

Further support of the involvement of brines in the El Arteal sinistral-normal fault segment stems from crystal morphologies of celestite and goethite observed in fault gouge samples from MA-2 (goethite; Figure 5d–f) and MA-3 (celestite, Figure 6d).

Rapid crystal growth of celestine and goethite is frequently manifested through acicular or fibrous morphologies, indicative of precipitation under conditions of elevated oversaturation and intense nucleation. In celestine, such needle-like or radial aggregates typically form in settings characterized by rapid fluid mixing, high Sr availability, or kinetically driven crystallization, as documented in early hydrothermal environments [88]. Similarly, acicular goethite develops under conditions of elevated Fe^{3+} activity and precipitation far from equilibrium, often associated with fluctuating redox states, rapid Fe^{2+} oxidation, or high solution oversaturation, factors that promote directional crystal growth [89,90]. These morphologies contrast with nodular or botryoidal (globular cluster) habits that

arise under slower, diffusion-controlled growth, underscoring the influence of kinetic parameters in mineral fabric development and offering valuable insights into the physicochemical evolution of the parent fluids [90,91]. The occurrence of microscale precipitates of iron oxides and oxyhydroxides within microfractures, phyllosilicates, or other host minerals in several samples from the Almagrera Range (F7 in MA-2 and F9 in MA-5-9 can be attributed to interaction with sulphate-rich acidic waters. According to Bigham and Nordstrom [92], acid sulphate waters generated by sulphide oxidation promote the precipitation of poorly crystalline Fe hydroxysulphates and oxyhydroxides. These minerals often nucleate heterogeneously on existing surfaces, including clay minerals and alteration products, forming nano- to microscale aggregates that can be present in trace amounts. Their presence indicates environments characterized by high sulphate activity, fluctuating redox conditions, and low pH, which are consistent with late-stage hydrothermal alteration or supergene processes affecting sulphide-rich ore bodies. Evidence of this phenomenon can be observed in the elevated levels of sulphates recorded in Almagrera Range waters in 1971, with concentrations reaching 7575 mg/L, comparable to those of chlorides and a pH of 2.9 (Table 1). Consequently, these textural features provide valuable evidence for the role of mineralogical changes and support interpretations of fluid evolution under strongly oxidizing conditions.

6.2. Geochemical Signature in the Fault Segment

The enrichment in large-ion lithophile elements (LILE), including Li, Rb, Cs, K, Sr, and Ba, observed along the fault segment (Figure 10a and Table 3), also indicates intense fluid–rock interaction under hydrothermal conditions. These highly mobile elements preferentially partition into aqueous fluids during metasomatic alteration, particularly in structurally controlled zones that act as conduits for deep-sourced fluids [93,94]. Their mobilization is commonly associated with acidic hydrothermal fluids capable of leaching feldspars and mica-group minerals, releasing alkaline and alkaline earth elements into solution. In contrast, HFSE and HREE, as observed in Figure 10c and Figure 10d, remain largely immobile due to their strong lattice bonding and low solubility [95].

LREE exhibits only slight enrichment, but these slight anomalies are linked to those of LILE (see Section 5.2). The most probable explanation is likely incorporation of these elements into the structure of neoformed illite, which, when precipitated from hydrothermal fluids, strongly concentrates Cs and, to a lesser extent, Rb. Srodon and Jewula [96] reported cesium concentrations 18 times those of average continental crust and Rb ones 2.5 times higher in anomalous illites that precipitated from the hydrothermal fluids. The maximum Cs concentration, although measured in whole rock, is 20 times the continental crust average (sample F7, Figure 10a) and is linked to the maximum abundance of phyllosilicates in the fault gouge samples, suggesting both illite control and a very important Rb and Li enrichments in the same and adjacent samples (MA-4, samples F6 to F8, Figure 10a), although less pronounced compared also to those reported by Srodon and Jewula [96]. In addition, the fault zone also shows enrichment in chalcophile elements such as As, Sb, Bi, and Cu. These elements typically concentrate in hydrothermal systems due to their strong affinity for sulphur and their incorporation into sulphide and sulphosalt phases during fluid–rock interaction [97,98]. Their presence suggests that the fault acted not only as a pathway for alkali-rich fluids but also as a place for sulphide precipitation, consistent with epithermal mineralization processes.

The Pearson correlation matrix in Section 5.3 reveals that very strong intra-group correlations among LREE and HREE, which contrasts with their weaker mutual correlations (e.g., La–Yb = 0.55; Ce–Dy = 0.66), could be due to different mineralogical control, i.e., different host mineral phases for each REE subgroup. The higher correlation between HREE-HFSE

(e.g., Nb–Yb = 0.90) suggests that both groups behaved similarly, as immobile elements during alteration, thus preserving the geochemical association linked to substitution in the structure of common accessory minerals in the metamorphic rocks, such as zircon and monazite [99], which were detected by XRD.

As for the LREE, the same phyllic alteration processes responsible for illite neoformation could have also triggered alteration of monazite, the signs of which were observed (Figures 6d and 7e). Poitrasson et al. [100] described how fluid-rock interaction at temperatures around 200 °C can result in replacement of P^{5+} + REE^{3+} by Si^{4+} and Th^{4+} in the monazite structure. This coupled substitution results in a disturbance of the phosphorous—oxygen network (due to P^{5+} loss) and a volume reduction of the 9-coordinated site in the monazite structure, such that the larger cations (LREE) are expelled while the smaller HREE are retained. This would explain both the observed positive correlation between LILE (Rb, Cs, K) and LREE, and the decoupling of the latter with respect to HREE.

Chalcophile elements and TTE (Fe, Mn, Ni, Co) present a variable correlation, especially Fe-chalcophile (Fe–Sb = 0.36; Fe–As = 0.71) pointing to alternating episodes of oxidation–reduction and sulphur availability, which controlled the precipitation of either oxide phases (hematite–goethite) or sulphide/sulphoarsenide assemblages (As, Sb-bearing minerals) during hydrothermal evolution of the system as documented in the historical mine geology of the area [43,101]. The non-significant correlations between oxide minerals and LILE are consistent with the decoupling of neoformed phyllosilicates formation processes, whereby LILE (Rb, Cs, K) are mobilised into neoformed phyllosilicates -rich halos and Fe is oxidised to magnetite, hematite, and goethite. These processes are often spatially and temporally distinct within hydrothermal alteration zones [102]. Another elemental assemblage is Ca-Sr-Ba, which is related to the presence of sulphates (gypsum, Ca; celestine, Sr; barite, Ba) in the mineral assemblage (MA-3 and MA-4).

6.3. The Hydrogeological Key

Hydrochemical sampling was conducted to verify previously reported historical anomalies, while pumping tests were not performed due to the potential risks and associated environmental impact. The resulting hydrochemical data from the Almagrera Range reveal the presence of three aquifers (Figure 12), rather than just two aquifers as Navarro and Carulla [36] had suggested: (1) a separate aquifer hosted in Quaternary deposits from sodium-sulfate waters, (2) a shallow aquifer hosted in Neogene marly sandstones with sodium–chloride hydrochemical facies and (3) a deep hypersaline aquifer circulating through fractured metamorphic rocks with high sodium–chloride hydrofacies.

The shallow (2) and deep (3) aquifers exhibit lateral and vertical variability, with evidence of mixing zones where chloride concentrations decrease, suggesting interaction between shallow and deep waters. A close examination of historical (Table 1) and current data sets (Table 4) reveals a robust correlation between total salinity (along with depth and temperature) and the concentration of Cl^{-}, Na^{+}, K^{+}, Li, Sr, and Rb. In contrast, sulphates and some alkaline earth elements (As, Bi, Cu, Ca, Mg, Ba) do not show a consistent relationship with salinity, a phenomenon likely attributable to their genesis above the oxidation front [67]. The shallow aquifer is characterised by elevated levels of silica, while the deep system exhibits signs of silica depletion, suggesting reprecipitation (presence of authigenic quartz, Figure 5c) as a consequence of hydrothermal processes. The findings of this study corroborate the prevailing hypothesis that temperature exerts a predominant influence on the anomalous chemistry of thermal waters, a phenomenon that has been documented in other European geothermal systems [2]. Geothermometric calculations in the deep investigation well yielded a mean geothermal gradient of 0.0675 $°C \cdot m^{-1}$

and reservoir temperatures of approximately 190 °C. These findings confirm equilibrium conditions for deep fluids [36].

The deep Na-Cl brines, which are enriched in Li, Rb, and Cs, bear a resemblance to those described in the Upper Rhine Graben or Campi Flegrei (Italy), where fault-controlled fluid flow and hydrothermal alteration drive lithium mobility [1,2,103]. In conditions of elevated total dissolved solids (TDS), formed by the evaporation and concentration of the brine, there is an enhancement in lithium concentration due to an increase in ionic strength [103]. The observed increase in boron concentrations (also coupled with the highest Li contents) toward the deepest sectors of the system and near the metamorphic basement suggests a strong geothermal influence on fluid evolution. Boron is widely recognized as a tracer of high-temperature water–rock interaction, particularly in geothermal environments where prolonged fluid residence times and interaction with metamorphic (pelitic) or felsic magmatic rocks enhance its mobilization [15,104], although boron sources may also depend on other climatic factors linked to salinity [105]. In the Almagrera range, tourmaline is an accessory mineral in phyllite-micaschists, whereas scattered outcrops of volcanic rocks piercing the metamorphic basement are composed of dacite and rhyodacite. Therefore, the interaction of hydrothermal fluids and either of the two rock types may have promoted boron enrichment in the sampled waters. Moreover, in felsic igneous rocks, boron is typically concentrated in the glassy groundmass, whereas lithium is incorporated in biotite and hornblende [106]. The latter are only weakly affected by hydrothermal alteration at low temperatures, so that the corresponding fluid will have high B/Li ratios. However, the sampled waters enriched in boron (SA samples, Table 4) exhibit low B/Li ratios (0.4), which would reflect high temperature alteration with Li release from ferromagnesian minerals. Additionally, elevated boron contents often correlate with chloride-rich fluids and have been used as geochemical indicators of deep circulation pathways and temperatures exceeding 200 °C [107].

The presence of Miocene volcanic systems provides a magmatic heat source, thereby enhancing hydrothermal convection and mineral alteration. This process is analogous to those documented in Italian geothermal provinces [108] and the Salton Sea field [109]. In the latter, the coexistence of acidic, sulphate-rich fluids and hypersaline brines in deep hydrothermal environments has been reported [110].

Last, but not least, the sampled waters with high chloride concentrations (ART-3 to SA samples, Table 4) show lithium and rubidium enrichment factors ranging from 13 to 149 and from 3.8 to 6.5, respectively, relative to seawater brine (0.4 mg/L Li and 0.2 mg/L Rb [111]. Although these enrichment factors are not so high as those reported from some salt lake brines [112], they are higher than those evaluated as potential resources from desalination plants [113], so more data would be desirable to fully constrain their economic potential.

6.4. Comparative Analysis of Hydrochemistry and Geochemistry in El Arteal Fault Segment

Fault-zone rocks and adjacent waters show coherent yet contrasting patterns that reflect element mobility under fault-controlled fluid–rock interaction and salinity/redox constraints. Rock samples (Table 3) from the fault core (F6–F8B) are enriched in alkalis (Li up to 84 ppm; Cs up to 98.8 ppm) with Rb > Cs (e.g., F7: 291 vs. 98.8 ppm, respectively). These rocks also show high Fe (to 12.9 wt%), Mn (to 5850 ppm in F2A), and Pb–Zn (up to 900 and 570 ppm, respectively), whereas Ca rises sharply in samples F10–F13 (up to 14.6 wt%) with Sr reaching 2030 ppm. LREE dominate the REE budget at the fault center (e.g., La = 51.6; Ce = 95.3 ppm) while MREE–HREE remain $\leq$~8 ppm (e.g., Gd = 7.9; Dy = 6.86 ppm). HFSE are broadly uniform along strike, and fault gouge (F3–F4) concentrates Sb–Cu–As (to 82.5–120–60 ppm).

Waters (Table 4) from deep wells and brines (ART-3/ART-4; S.A.) carry very high dissolved Li (brines ~60 mg/L) as well as abundant Ca–Sr (S.A. > 5000 mg/L Ca; ≤186 mg/L Sr), whereas Fe is generally low (<0.15 mg/L) and Mn is minor except at ART-4 (22 mg/L). Zn is usually below the detection limit but reaches 3660 µg/L at ART-4. Rb and Cs concentrations are of similar magnitude in the most mineralized waters (e.g., ART-3: 3.5 mg/L; ART-4: 3.2 mg/L). In turn, dissolved REE are extremely low (e.g., ART-3: La = 0.005 µg/L; Ce = 0.062 µg/L), Y is only sporadically detected (0.074 µg/L in ART-4), and U varies markedly (20.7 µg/L in ART-1 vs. 3.44 µg/L near the Nevado-Filábride Complex) (Table 4). Collectively, these data indicate that the fault core acts as a rock-hosted reservoir for Li–Cs–Rb, Fe–Mn, Ca–Sr, Pb–Zn (and Sb–Cu–As in fault gouge), whereas deep, saline flow paths selectively mobilize the most soluble and exchange-prone cations (notably Li and Ca–Sr) and locally enhance Mn and Zn where redox shifts or mixing occur. The depressed aqueous REE mirrors the rock's LREE-skewed inventory, pointing to efficient adsorption and limited complexation under the prevailing conditions.

7. Conclusions

The El Arteal fault segment, within the eastern PFZ strand, is a significant surface manifestation of the geothermal and hydrothermal processes that have impacted the southernmost region of the tectono-magmatic Águilas Arc system, located within the NVP. The data show noticeable evidence of multiple stages of rock-fluid interaction, resulting from circulation of distinct fluids mobilized from shallow sources and deep geothermal sources. Hydrothermal alteration processes are revealed by changes in fault gouge mineralogy and geochemistry compared to those from reference rock samples, as well as the hydrochemistry of the waters from the well and mine shafts sampled in the area. It was determined that six distinct MA were present within the fault segment, where the fault gouge samples differed from the reference samples in terms of cataclastic and mylonitic textures, as well as the occurrence of authigenic minerals such as halite, kaolinite, illite, paragonite, hematite, gypsum, goethite, barite, celestine, and quartz. Most quartz, muscovite, and accessory minerals such as tourmaline, zircon, rutile, and monazite are included as inherited minerals from the host rocks. The analysis of geochemical and hydrochemical data has revealed the presence of elevated levels of large-ion lithophile elements (LILE) and minor chalcophile and LREE enrichment. Three aquifers were identified from hydrochemical data: The first aquifer is hosted in Quaternary deposits and is characterised by sodium-sulfate waters. The second aquifer is a shallow aquifer hosted in Neogene marly sandstones with mixed sodium–chloride waters. The third aquifer is a deep hypersaline aquifer circulating through fractured metamorphic rocks with high sodium–chloride hydrofacies. The deep aquifer is characterised by elevated levels of conductivity and temperature, as well as high concentrations of sodium (Na^+) and chloride (Cl^-) ions. In addition, there is anomalous enrichment in several key alkaline metals (Li, Rb, and Cs) in the deeper and more internal sectors of the Almagrera Range. The values suggest extraction potential, although more data are required to assess its economic viability. These findings are consistent with a model of multiple-stage fluid-rock interaction controlled by temperature. The first stage involved widespread epithermal mineralisation in the Almagrera Range, driven by acidic, sulphate-rich waters resulting from sulphide oxidation. These waters precipitated iron-bearing minerals and chalcophile elements (As, Bi, Cu, Pb, Sb). This phase was characterised by slow crystal growth, forming nodular or botryoidal goethite and subhedral hematite. This was followed by rapid fluid mixing and high supersaturation, generating acicular goethite and celestine, as well as microscale iron oxide precipitates. A later stage was dominated by the circulation of hypersaline, acidic to neutral fluids enriched in Li, Rb, Cs, and Sr, which led to the formation of halite, gypsum, and paragonite. These fluid types caused feldspar alteration and

phyllosilicates and clay mineral formation, reflecting metasomatic processes. The lithium and cesium enrichment observed in the Almagrera Range region is likely attributable to a combination of magmatic heat driving, brine circulation, and feldspar–mica alteration along fault zones. This evolution provides an abnormal geochemical signature that is unique in the Aguilas Arc Geothermal System.

Author Contributions: Conceptualization, E.R.-F., M.P., C.D.I., Á.S.-M. and E.S.-R.; methodology, E.R.-F.; software, E.R.-F. and M.P.; validation, M.P., C.D.I., Á.S.-M., E.S.-R. and L.V.; formal analysis, E.R.-F., M.P., C.D.I., Á.S.-M. and E.S.-R.; investigation, E.R.-F., M.P., C.D.I., Á.S.-M. and E.S.-R.; resources, M.P., C.D.I., Á.S.-M., E.S.-R. and L.V.; data curation, E.R.-F., M.P., C.D.I., Á.S.-M. and E.S.-R.; writing—original draft preparation, E.R.-F.; writing—review and editing, E.R.-F., M.P., C.D.I., Á.S.-M., E.S.-R. and L.V.; visualization, E.R.-F.; supervision, M.P., C.D.I., Á.S.-M. and E.S.-R.; funding acquisition, Á.S.-M., E.S.-R. and L.V. All authors have read and agreed to the published version of the manuscript.

Funding: The present research was funded by MICIU/AEI/10.13039/501100011033 within the framework of the scholarship DIN2022-012822. In addition, financial support was provided by MINERALES Y PRODUCTOS DERIVADOS S.A. (MINERSA) and Geomnia Natural Resources S.L.N.E.

Institutional Review Board Statement: Not applicable.

Informed Consent Statement: Not applicable.

Data Availability Statement: The data presented in this study are available on request from the corresponding author.

Acknowledgments: The authors gratefully acknowledge all individuals who contributed to the successful completion of this research. We extend special thanks to Salvador and Martín, local collaborators from the El Arteal dewatering system and mine area, whose assistance was crucial for conducting the geological and hydrogeological investigations. We also express our appreciation to Marian, Pedro, and Carmen, technicians at Laboratory of the Department of Petrology and Mineralogy, Faculty of Geology, Complutense University of Madrid, for their expertise and support in preparing the thin sections essential for mineralogical analyses, as well as the technicians Miriam, Carlos, Isidoro, and Noemí from the Interdepartmental Research Service of the Autonomous University of Madrid (Spain). Finally, we acknowledge MINERALES Y PRODUCTOS DERIVADOS S.A. (MINERSA) for providing financial and technical support, which was fundamental to the development of this study.

Conflicts of Interest: Authors Elena Real-Fernández, Ángel Sánchez-Malo and Enrique Sanz-Rubio were employed by the company Geomnia Natural Resources, SLNE. Author Luis Villa was employed by the company Minersa Group. The remaining authors declare that the research was conducted in the absence of any commercial or financial relationships that could be construed as a potential conflict of interest. The authors declare that this study received funding from MINERALES Y PRODUCTOS DERIVADOS S.A. (MINERSA) and Geomnia Natural Resources S.L.N.E. The funder had the following involvement with the study in the validation, investigation, resources, review, editing and supervision.

Abbreviations

The following abbreviations are used in this manuscript:

PFZ	Palomares Fault Zone
TASZ	Trans-Alboran Shear Zone
EBSZ	Eastern Betic Shear Zone
HP–LT	High-Pressure/Low-Temperature
NVP	Neogene Volcanic Province

LILE	Large Ion Lithophile Elements
HFSE	High Field Strength Elements
LREE	Light Rare-Earth Elements
HREE	Heavy Rare-Earth Elements
TTE	Transition Trace Elements
SEM	Scanning Electron Microscopy
BSE	Backscattered Electrons
SE	Secondary Electrons
ICP-MS	Inductively Coupled Plasma Mass Spectrometry
ICP-AES	Inductively Coupled Plasma–Atomic Emission Spectroscopy
XRD	X-Ray Diffraction
D.L.	Detection Limits
MA	Mineral Assemblages
TDS	Total Dissolved Solids
RS	Reference Samples

References

1. Liu, M.; Kong, Y.; Guo, Q. Sources and Enrichment Mechanisms of Lithium, Rubidium, and Cesium in Waters of Magmatic-Hydrothermal Systems. *Earth-Sci. Rev.* **2025**, *270*, 105241. [CrossRef]
2. Sanjuan, B.; Gourcerol, B.; Millot, R.; Rettenmaier, D.; Jeandel, E.; Rombaut, A. Lithium-Rich Geothermal Brines in Europe: An up-Date about Geochemical Characteristics and Implications for Potential Li Resources. *Geothermics* **2022**, *101*, 102385. [CrossRef]
3. Szanyi, J.; Rybach, L.; Abdulhaq, H.A. Geothermal Energy and Its Potential for Critical Metal Extraction—A Review. *Energies* **2023**, *16*, 7168. [CrossRef]
4. Shu, Q.; Deng, J. The Composition of Magmatic-Hydrothermal Fluids and Their Related Metal Mineralization. *Sci. China Earth Sci.* **2025**, *68*, 208–225. [CrossRef]
5. Wu, H.; Yang, H.; Zhu, Y.S.; Ge, W.C.; Ji, Z.; Jing, Y.; Zhang, Z.C. How Do Fluids Control Beryllium Mineralization in a Magmatic-Hydrothermal System: Evidence from Mica Geochemistry and Quartz-Beryl O Isotopes. *Am. Mineral.* **2025**. [CrossRef]
6. Addleman, R.S. *Recovery of Rare Earths, Precious Metals and Other Critical Materials from Geothermal Waters with Advanced Sorbent Structures—CRADA 355 (Abstract)*; Pacific Northwest National Laboratory: Richland, WA, USA, 2025; p. 5.
7. Pawar, R.; Santara, S.; Sircar, A.; Kumari, R.; Bist, N.; Yadav, K. Extraction of Salt and Base Metals from Geothermal Water: Kinetic Modeling and Mechanism. *MRS Energy Sustain.* **2023**, *10*, 219–237. [CrossRef]
8. Audétat, A. The Metal Content of Magmatic-Hydrothermal Fluids and Its Relationship to Mineralization Potential. *Econ. Geol.* **2019**, *114*, 1033–1056. [CrossRef]
9. Faulds, J.; Coolbaugh, M.; Bouchot, V.; Moeck, I.; Oğuz, K. *Characterizing Structural Controls of Geothermal Reservoirs in the Great Basin, USA, and Western Turkey: Developing Successful Exploration Strategies in Extended Terranes*; World Geothermal Congress: Bali, Indonesia, 2010; p. 11.
10. Faulkner, D.R.; Mitchell, T.M.; Rutter, E.H.; Cembrano, J. On the Structure and Mechanical Properties of Large Strike-Slip Faults. In *The Internal Structure of Fault Zones: Implications for Mechanical and Fluid-Flow Properties*; Wibberley, C.A.J., Kurz, W., Imber, J., Holdsworth, R.E., Collettini, C., Eds.; Geological Society of London: London, UK, 2008; Volume 299, pp. 139–150.
11. Faulkner, D.R.; Jackson, C.A.L.; Lunn, R.J.; Schlische, R.W.; Shipton, Z.K.; Wibberley, C.A.J.; Withjack, M.O. A Review of Recent Developments Concerning the Structure, Mechanics and Fluid Flow Properties of Fault Zones. *J. Struct. Geol.* **2010**, *32*, 1557–1575. [CrossRef]
12. Schleicher, A.M.; Van Der Pluijm, B.A.; Warr, L.N. Nanocoatings of Clay and Creep of the San Andreas Fault at Parkfield, California. *Geology* **2010**, *38*, 667–670. [CrossRef]
13. Sibson, R.H. Structural Permeability of Fluid-Driven Fault-Fracture Meshes. *J. Struct. Geol.* **1996**, *18*, 1031–1042. [CrossRef]
14. Audétat, A.; Edmonds, M. Magmatic-Hydrothermal Fluids. *Elements* **2020**, *16*, 401–406. [CrossRef]
15. Giggenbach, W.F. Isotopic Shifts in Waters from Geothermal and Volcanic Systems along Convergent Plate Boundaries and Their Origin. *Earth Planet. Sci. Lett.* **1992**, *113*, 495–510. [CrossRef]
16. Abad, I.; Jiménez-Millán, J.; Sánchez-Roa, C.; Nieto, F.; Velilla, N. Neocrystallization of Clay Minerals in the Alhama de Murcia Fault (Southeast Spain): Implications for Fault Mechanics. *Clay Miner.* **2019**, *54*, 1–13. [CrossRef]
17. Abad, I.; Nieto, F.; Reolid, M.; Jiménez-Millán, J. Evidence of Phyllosilicate Alteration Processes and Clay Mineral Neoformation Promoted by Hydrothermal Fluids in the Padul Fault Area (Betic Cordillera, SE Spain). *Appl. Clay Sci.* **2022**, *230*, 106669. [CrossRef]

18. Dyja, V.; Hibsch, C.; Tarantola, A.; Cathelineau, M.; Boiron, M.-C.; Marignac, C.; Bartier, D.; Carrillo-Rosúa, J.; Ruano, S.M.; Boulvais, P. From Deep to Shallow Fluid Reservoirs: Evolution of Fluid Sources during Exhumation of the Sierra Almagrera, Betic Cordillera, Spain. *Geofluids* **2016**, *16*, 103–128. [CrossRef]
19. Haines, S.; Lynch, E.; Mulch, A.; Valley, J.W.; van der Pluijm, B. Meteoric Fluid Infiltration in Crustal-Scale Normal Fault Systems as Indicated by δ18O and δ2H Geochemistry and 40Ar/39Ar Dating of Neoformed Clays in Brittle Fault Rocks. *Lithosphere* **2016**, *8*, 587–600. [CrossRef]
20. Hanson, R.B. Hydrodynamics of Magmatic and Meteoric Fluids in the Vicinity of Granitic Intrusions. *Earth Environ. Sci. Trans. R. Soc. Edinb.* **1996**, *87*, 251–259. [CrossRef]
21. Weis, P. The Dynamic Interplay between Saline Fluid Flow and Rock Permeability in Magmatic-Hydrothermal Systems. *Geofluids* **2015**, *15*, 350–371. [CrossRef]
22. Coppier, G.; Griveaud, P.; De Larouziere, F.-D.; Montenat, C.; Ott d'Estevou, P. Example of Neogene Tectonic Indentation in the Eastern Betic Cordilleras: The Arc of Aguilas (Southeastern Spain). *Geodin. Acta* **1989**, *3*, 37–51. [CrossRef]
23. Sanz De Galdeano, C. Geologic Evolution of the Betic Cordilleras in the Western Mediterranean, Miocene to the Present. *Tectonophysics* **1990**, *172*, 107–119. [CrossRef]
24. Sanz de Galdeano, C.; Azañón, J.M.; Cabral, J.; Ruano, P.; Alfaro, P.; Canora, C.; Ferrater, M.; García-Tortosa, F.J.; García-Myordomo, J.; Grácia, E.; et al. Active Faults in the Betic Cordillera. In *The Geology of Iberia: A Geodynamic Approach: Volume 5: Active Processes: Seismicity, Active Faulting and Relief*; Quesada, C., Oliveira, J.T., Eds.; Regional Geology Reviews; Springer Nature: Cham, Switzerland, 2020; Volume 5, pp. 56–75.
25. Tendero-Salmerón, V.; Ercilla, G.; González-Castillo, L.; Madarieta-Txurruka, A.; Martínez-Moreno, F.J.; Estrada, F.; Galindo-Zaldivar, J. Gravimetric Survey and Modelling of a Tectonic Indenter Boundary: The Palomares Fault Zone (Betic Cordillera, Iberia). *Tectonophysics* **2024**, *872*, 230147. [CrossRef]
26. Weijermars, R. The Palomares Brittle—Ductile Shear Zone of Southern Spain. *J. Struct. Geol.* **1987**, *9*, 139–157. [CrossRef]
27. Instituto Geológico y Minero de España (IGME); Empresa Nacional Adaro de Investigaciones Mineras (ENADIMSA). *Investigación de las Posibilidades de Existencia de Energía Geotérmica en la Comarca de Mazarrón–Águilas (Murcia). Tomo I.*; IGME: Madrid, Spain, 1985; pp. 1–29.
28. De Larouzière, F.D.; Bolze, J.; Bordet, P.; Hernandez, J.; Montenat, C.; Ott d'Estevou, P. The Betic Segment of the Lithospheric Trans-Alboran Shear Zone during the Late Miocene. *Tectonophysics* **1988**, *152*, 41–52. [CrossRef]
29. Somoza, L.; Medialdea, T.; Terrinha, P.; Ramos, A.; Vázquez, J.-T. Submarine Active Faults and Morpho-Tectonics Around the Iberian Margins: Seismic and Tsunamis Hazards. *Front. Earth Sci.* **2021**, *9*, 653639. [CrossRef]
30. López Ruiz, J.; Rodríguez Badiola, E. La Region Volcánica Neogena del Sureste de España. *Estud. Geológicos* **1980**, *36*, 5–63.
31. Casalini, M.; Avanzinelli, R.; Tommasini, S.; Natali, C.; Bianchini, G.; Prelević, D.; Mattei, M.; Conticelli, S. Petrogenesis of Mediterranean Lamproites and Associated Rocks: The Role of Overprinted Metasomatic Events in the Post-Collisional Lithospheric Upper Mantle. In *Lamprophyres, Lamproites and Related Rocks: Tracers to Supercontinent Cycles and Metallogenesis*; Krmíček, L., Chalapathi Rao, N.V., Eds.; Geological Society of London: London, UK, 2022; ISBN 978-1-78620-543-8.
32. Torne, M.; Jiménez-Munt, I.; Negredo, A.M.; Fullea, J.; Vergés, J.; Marzán, I.; Alcalde, J.; Gómez-Rivas, E.; de la Noceda, C.G. Advances in the Modeling of the Iberian Thermal Lithosphere and Perspectives on Deep Geothermal Studies. *Geotherm Energy* **2023**, *11*, 3. [CrossRef]
33. Alonso-Chaves, F.M.; Andreo, B.; Arias, C.; Azañón, J.M.; Balanyá, J.C.; Barón, A.; Booth-Rea, G.; Castro, J.M.; Chacón, B.; Company, M.; et al. Cordillera Bética y Baleares. In *Geología de España*; Vera, J.A., Ed.; IGME: Madrid, Spain, 2004; pp. 346–464.
34. Colmenar-Santos, A.; Folch-Calvo, M.; Rosales-Asensio, E.; Borge-Diez, D. The Geothermal Potential in Spain. *Renew. Sustain. Energy Rev.* **2016**, *56*, 865–886. [CrossRef]
35. Instituto Geológico y Minero de España (IGME). *La Energía Geotérmica*; IGME: Madrid, Spain, 1985.
36. Navarro, A.; Carulla, N. Evaluation of Geothermal Potential in the Vicinity of the Flooded Sierra Almagrera Mines (Almeria, SE Spain). *Mine Water Env.* **2018**, *37*, 137–150. [CrossRef]
37. Booth-Rea, G.; Azañón, J.M.; García-Dueñas, V.; Augier, R. Uppermost Tortonian to Quaternary Depocentre Migration Related with Segmentation of the Strike-Slip Palomares Fault Zone, Vera Basin (SE Spain). *C. R. Geosci.* **2003**, *335*, 751–761. [CrossRef]
38. Booth-Rea, G.; Azañón, J.-M.; Azor, A.; García-Dueñas, V. Influence of Strike-Slip Fault Segmentation on Drainage Evolution and Topography. A Case Study: The Palomares Fault Zone (Southeastern Betics, Spain). *J. Struct. Geol.* **2004**, *26*, 1615–1632. [CrossRef]
39. Arribas Rosado, A.; Arribas Moreno, A. Caracteres metalogénicos y geoquímica isotópica del azufre y el plomo de los yacimientos de minerales metálicos del sureste de España. *Boletín Geológico Y Min.* **1995**, *106*, 23–62.
40. Martinez-Frías, J. Sulphide and sulphosalt mineralogy and paragenesis from the Sierra Almagrera veins, Betic Cordillera (SE Spain). *Estud. Geológicos* **1991**, *47*, 271–279. [CrossRef]
41. López-Gutiérrez, J.; Martínez-Frías, J.; Lunar, R.; López-García, J.A. El Rombohorst mineralizado de Las Herrerias: Un caso de «doming» e hidrotermalismo submarino mioceno en el SE ibérico. *Estud. Geológicos* **1993**, *49*, 13–19. [CrossRef]

42. Mata Perelló, J.M. Recorrido geológico y minero por las comarcas de Sorbas, Vera y Cuevas de Almanzora: Desde la Venta del Pobre a Cuevas de Almanzora y a la Sierra de Almagrera. *Algeps Rev. Geol.* **2011**, *XXXVIII*, 1–8. [CrossRef]
43. Navarro, A. Posible aprovechamiento geotérmico del drenaje minero en Sierra Almagrera (Almería). *Re Met.* **2018**, *30*, 89–102.
44. Navarro, A. Las Aguas Termales de Sierra Almagrera: De Un Problema Histórico En El Desarrollo de La Actividad Minera a Un Recurso Por Explotar. In *Geología y Minería en Los Siglos XIX y XX: Paisajes, Historia y Patrimonio. Actas Del XIX Congreso Internacional Sobre Patrimonio Geológico y Minero*; Ayarzagüen Sanz, M., Fernández Bolea, E., López Cidad, J.F., Sebastián Pérez, M.Á., Eds.; Sociedad Española para la Defensa del Patrimonio Geológico y Minero (SEDPGYM): Almería, Spain, 2023; pp. 60–80.
45. Sánchez Martos, F.; Alonso Blanco, J.M.; Calaforra Chordi, J.M. Encuadre geológico de la provincia de Almería. In *Problemática de la Gestión del Agua en Regiones Semiáridas*; Instituto de Estudios Almerienses: Almería, Spain, 2001; pp. 15–28, ISBN 84-8108-240-6.
46. Artero García, J.M. Síntesis geológico-minera de la provincia de Almería. *Boletín Inst. Estud. Almerienses. Cienc.* **1986**, 57–79.
47. Booth-Rea, G.; Azañón, J.M.; Goffé, B.; Vidal, O.; Martínez-Martínez, J.M. High-Pressure, Low-Temperature Metamorphism in Alpujarride Units of Southeastern Betics (Spain). *C. R. Géosci.* **2002**, *334*, 857–865. [CrossRef]
48. Stokes, M. Plio-Pleistocene Drainage Development in an Inverted Sedimentary Basin: Vera Basin, Betic Cordillera, SE Spain. *Geomorphology* **2008**, *100*, 193–211. [CrossRef]
49. Augier, R.; Jolivet, L.; Robin, C. Late Orogenic Doming in the Eastern Betic Cordilleras: Final Exhumation of the Nevado-Filabride Complex and Its Relation to Basin Genesis. *Tectonics* **2005**, *24*, TC4003. [CrossRef]
50. Booth-Rea, G.; Azañón, J.M.; Martínez-Martínez, J.M.; Vidal, O.; García-Dueñas, V. Contrasting Structural and P-T Evolution of Tectonic Units in the Southeastern Betics: Key for Understanding the Exhumation of the Alboran Domain HP/LT Crustal Rocks (Western Mediterranean). *Tectonics* **2005**, *24*, TC2009. [CrossRef]
51. Montenat, C.; Bizon, G.; Bizon, J.-J.; Carbonnel, G.; Muller, C.; Reneville, P.D. Continuité ou discontinuité de sémentation marine mio-pliocène en Méditerranée occidentale. L'example du bassin de vera (Espagne méridionale). *Rev. Inst. Fr. Pét.* **1976**, *31*, 613–664. [CrossRef]
52. Ott d'Estevou, P.; Montenat, C.; Alvado, J.C. Le Bassin de Vera-Garrucha. In *Les Bassins Néogeènes du Domaine Beétique Orientale (Espagne)*; Documents et Travaux du Institut Géologique Albert-de-Lapparent 12–13; Institut Géologique Albert-de-Lapparent: Paris, France, 1990; pp. 165–187.
53. Sánchez-Bellón, A.; Mosser, C.; Roquin, C.; Pardo-Sebastián, E. Geochemical Characterization of Sedimentary Basins by Statistical Analysis: The Mio-Pliocene Sequences of the Vera Basin, SE Spain. *Chem. Geol.* **1994**, *116*, 229–243. [CrossRef]
54. Martínez-Martínez, J.M.; Azañón, J.M. Mode of Extensional Tectonics in the Southeastern Betics (SE Spain): Implications for the Tectonic Evolution of the Peri-Alborán Orogenic System. *Tectonics* **1997**, *16*, 205–225. [CrossRef]
55. Platt, J.P.; Vissers, R.L.M. Extensional Collapse of Thickened Continental Lithosphere: A Working Hypothesis for the Alboran Sea and Gibraltar Arc. *Geology* **1989**, *17*, 540–543. [CrossRef]
56. Weijermars, R.; Roep, T.B.; Eeckhout, B.V.d.; Postma, G.; Kleverlaan, K. Uplift History of a Betic Fold Nappe Inferred from Neogene-Quaternary Sedimentation and Tectonics (in the Sierra Alhamilla and Almeria, Sorbas and Tabernas Basins of the Betic Cordilleras, SE Spain). *Neth. J. Geosci.* **1985**, *56*, 397–411.
57. Weijermars, R. Geology and Tectonics of the Betic Zone, SE Spain. *Earth-Sci. Rev.* **1991**, *31*, 153–236. [CrossRef]
58. Martínez-Martínez, J.M.; Soto, J.I.; Balanyá, J.C. Orthogonal Folding of Extensional Detachments: Structure and Origin of the Sierra Nevada Elongated Dome (Betics, SE Spain). *Tectonics* **2002**, *21*, 3-1-3-20. [CrossRef]
59. Tendero-Salmerón, V.; Ercilla, G.; González-Castillo, L.; Madarieta-Txurruka, A.; Martínez-Moreno, F.J.; Estrada, F.; Galindo-Zaldívar, J. Influencia de la zona de falla de Palomares en las cuencas adyacentes mediante prospección gravimétrica. *Geotemas* **2024**, 600.
60. Booth Rea, G.; Azañón, J.M.; Martínez-Martínez, J.M.; Vidal, O.; García-Dueñas, V. Análisis estructural y evolución tectonometamórfica del basamento de las cuencas neógenas de Vera y Huércal-Overa, Béticas orientales. *Rev. Soc. Geológica España* **2003**, *16*, 193–211.
61. Álvarez, F.; Aldaya, F. Las unidades de la Zona Bética en la región de Aguilas-Mazarrón (prov. de Murcia). *Estud. Geológicos* **1985**, *41*, 139–148. [CrossRef]
62. Martinez-Frías, J.; García-Guinea, J.; López-Ruiz, J.; López-García, J.Á.; Benito-García, R. Las mineralizaciones epitermales de Sierra Almagrera y de la cuenca de Herrerías, Cordilleras Béticas. *Boletín Soc. Española Mineral.* **1989**, *12*, 261–271.
63. Martínez-Frías, J.; García-Guinea, J. Yacimientos de plata y chimeneas submarinas asociadas del área de Cuevas de Almanzora. In *Recursos Naturales y Medio Ambiente de Cuevas del Almanzora*; García Rossell, L., Martínez-Frías, J., Eds.; Instituto de Estudios Almerienses: Almería, Spain, 1993; pp. 237–262.
64. Morales Ruano, S. Mineralogía, Geoquímica y Metalogenia de Los Yacimientos Hidrotermales del Sureste de España (Águilas-Sierra Almagrera). Ph.D. Thesis, Universidad de Granada, Granada, Spain, 1994.
65. Font, X.; Rodríguez, P.; Navarro Flores, A.; Viladevall Solé, M. Las mineralizaciones auríferas de Sierra Almagrera (Almería): Estudio geoquímico y modelos de yacimientos. *Boletín Geológico Min.* **1994**, *105*, 85–101.

66. Trio Maseda, M.; Guillermo Ortuño, M. *BARIO06: Panorama Nacional de Producción Minera de Barita*; Instituto Geológico y Minero de España (IGME): Madrid, Spain, 2006; pp. 1–6.
67. Carulla, N. Contribución al Conocimiento de la Dinámica Hidrogeólogica en Clima Semiárido Depresion de Vera (Almería). Ph.D. Thesis, Universitat Autònoma de Barcelona, Bellaterra, Spain, 1978.
68. Gómez Iribarne, B. *Estadística Minera de España*; Consejo de Minería, Ministerio de Fomento, Dirección General de Agricultura, Industria y Comercio: Madrid, Spain, 1908; pp. 142–149.
69. Carulla, N. Las salmueras mineras, termales y litiníferas de Sierra Almagrera (N.E. Almería). *Geotemas* **2012**, 930–933.
70. Ovejero, G. *Aguas Mineralizadas de Almagrera—Sondeo de Investigación. Informe Anual*; Peñarroya—MASA: Almería, Spain, 1982; pp. 1–4.
71. Alcalá, F.J.; Custodio, E. Using the Cl/Br Ratio as a Tracer to Identify the Origin of Salinity in Aquifers in Spain and Portugal. *J. Hydrol.* **2008**, *359*, 189–207. [CrossRef]
72. Santamaría-López, Á.; Abad, I.; Nieto, F.; Galdeano, C.S.d.; Santamaría-López, Á.; Abad, I.; Nieto, F.; Galdeano, C.S. de Early Mylonitization in the Nevado-Filábride Complex (Betic Cordillera) during the High-Pressure Episode: Petrological, Geochemical and Thermobarometric Data. *Minerals* **2022**, *13*, 24. [CrossRef]
73. Moore, D.M.; Reynolds, R.C., Jr. *X-Ray Diffraction and the Identification and Analysis of Clay Minerals*; Oxford University Press: New York, NY, USA, 1989; ISBN 10: 0195087135.
74. Schultz, L.G. *Quantitative Interpretation of Mineralogical Composition from X-Ray and Chemical Data for the Pierre Shale*; U.S. Geological Survey Professional Paper 391; United States Government Printing Office: Washington, DC, USA, 1964; pp. C1–C31. [CrossRef]
75. Van der Marei, H.W. Quantitative Analysis of Clay Minerals and Their Admixtures. *Contr. Mineral. Petrol.* **1966**, *12*, 96–138. [CrossRef]
76. Whitney, D.L.; Evans, B.W. Abbreviations for Names of Rock-Forming Minerals. *Am. Mineral.* **2010**, *95*, 185–187. [CrossRef]
77. Priem, H.N.A.; Boelrijk, N.A.J.M.; Hebeda, E.H.; Verschure, R.M. Isotopic Age Determinations on Tourmaline Granite-Gneiss and a Metagranite in the Eastern Betic Cordilleras, SE Spain. *Geol. Mijnb.* **1966**, *45*, 184–187.
78. Rudnick, R.L.; Gao, S. Composition of the Continental Crust. In *Treatise on Geochemistry*; Elsevier: Amsterdam, The Netherlands, 2014; pp. 1–51.
79. Putnis, A. Mineral Replacement Reactions: From Macroscopic Observations to Microscopic Mechanisms. *Mineral. Mag.* **2002**, *66*, 689–708. [CrossRef]
80. Wintsch, R.P.; Christoffersen, R.; Kronenberg, A.K. Fluid-Rock Reaction Weakening of Fault Zones. *J. Geophys. Res. Solid Earth* **1995**, *100*, 13021–13032. [CrossRef]
81. Inoue, A.; Kitagawa, R. Morphological Characteristics of Illitic Clay Minerals from a Hydrothermal System. *Am. Mineral.* **1994**, *79*, 700–711.
82. Fulignati, P. Clay Minerals in Hydrothermal Systems. *Minerals* **2020**, *10*, 919. [CrossRef]
83. Brindley, G.W.; Brown, G. *Crystal Structures of Clay Minerals and Their X-Ray Identification*; Mineralogical Society of Great Britain and Ireland: Middlesex, UK, 1980; Volume 5, ISBN 978-0-903056-37-3.
84. Ece, Ö.I.; Ercan, H.Ü. Global Occurrence, Geology and Characteristics of Hydrothermal-Origin Kaolin Deposits. *Minerals* **2024**, *14*, 353. [CrossRef]
85. Abad, I.; Jiménez-Millán, J.; Schleicher, A.M.; van der Pluijm, B.A. Mineral Characterization, Clay Quantification and Ar–Ar Dating of Faulted Schists in the Carboneras and Palomares Faults (Betic Cordillera, SE Spain). *Eur. J. Mineral.* **2017**, *29*, 17–34. [CrossRef]
86. Jiménez-Millán, J.; Abad, I.; Hernández-Puentes, P.; Jiménez-Espinosa, R. Influence of Phyllosilicates and Fluid–Rock Interaction on the Deformation Style and Mechanical Behaviour of Quartz-Rich Rocks in the Carboneras and Palomares Fault Areas (SE Spain). *Clay Miner.* **2015**, *50*, 619–638. [CrossRef]
87. Gruner, J.W. Conditions for the Formation of Paragonite. *Am. Mineral.* **1942**, *27*, 131–134.
88. Tekin, E.; Varol, B.; Ayan, Z.; Satir, M. Epigenetic Origin of Celestite Deposits in the Tertiary Sivas Basin: New Mineralogical and Geochemical Evidence. *Neues Jahrb. Für Mineral.-Monatshefte* **2002**, *2002*, 289–318. [CrossRef]
89. Cornell, R.M.; Schwertmann, U. Formation. In *The Iron Oxides: Structure, Properties, Reactions, Occurences and Uses*; John Wiley & Sons, Ltd.: Hoboken, NJ, USA, 2003; pp. 345–364, ISBN 978-3-527-60209-4.
90. Schwertmann, U.; Friedl, J.; Stanjek, H. From Fe(III) Ions to Ferrihydrite and Then to Hematite. *J. Colloid Interface Sci.* **1999**, *209*, 215–223. [CrossRef]
91. Cornell, R.M.; Schwertmann, U. Crystal Morphology and Size. In *The Iron Oxides: Structure, Properties, Reactions, Occurences and Uses*; John Wiley & Sons, Ltd.: Hoboken, NJ, USA, 2003; pp. 59–94, ISBN 978-3-527-60209-4.
92. Bigham, J.M.; Nordstrom, D.K. Iron and Aluminum Hydroxysulfates from Acid Sulfate Waters. *Rev. Mineral. Geochem.* **2000**, *40*, 351–403. [CrossRef]
93. Bruhn, R.L.; Parry, W.T.; Yonkee, W.A.; Thompson, T. Fracturing and Hydrothermal Alteration in Normal Fault Zones. *Pure Appl. Geophys.* **1994**, *142*, 609–644. [CrossRef]

94. Zheng, Y.-F. Subduction Zone Geochemistry. *Geosci. Front.* **2019**, *10*, 1223–1254. [CrossRef]
95. Zhong, R.; Zhang, M.; Yu, C.; Cui, H. The Fluid Mobilities of K and Zr in Subduction Zones: Thermodynamic Constraints. *Minerals* **2021**, *11*, 394. [CrossRef]
96. Środoń, J.; Jewuła, K. Controls over Cesium and Rubidium Contents of Sedimentary Rocks. *Chem. Geol.* **2025**, *683*, 122745. [CrossRef]
97. Hedenquist, J.W.; Lowenstern, J.B. The Role of Magmas in the Formation of Hydrothermal Ore Deposits. *Nature* **1994**, *370*, 519–527. [CrossRef]
98. Heinrich, C.A. The Physical and Chemical Evolution of Low-Salinity Magmatic Fluids at the Porphyry to Epithermal Transition: A Thermodynamic Study. *Min. Depos.* **2005**, *39*, 864–889. [CrossRef]
99. Cherniak, D.J. Diffusion in Accessory Minerals: Zircon, Titanite, Apatite, Monazite and Xenotime. *Rev. Mineral. Geochem.* **2010**, *72*, 827–869. [CrossRef]
100. Poitrasson, F.; Chenery, S.; Bland, D.J. Contrasted Monazite Hydrothermal Alteration Mechanisms and Their Geochemical Implications. *Earth Planet. Sci. Lett.* **1996**, *145*, 79–96. [CrossRef]
101. Abdel-Halim, A.H. Hydrothermal Alteration of Ni-Rich Sulfides in Peridotites of Abu Dahr, Eastern Desert, Egypt: Relationships among Minerals in the Fe-Ni-Co-O-S System, f_{O2} and f_{S2}. *Am. Mineral.* **2023**, *108*, 614–633. [CrossRef]
102. Berger, B.R. Hydrothermal Alteration. In *Geochemistry*; Springer: Dordrecht, The Netherlands, 1998; pp. 331–333, ISBN 978-1-4020-4496-0.
103. Sanjuan, B.; Millot, R.; Innocent, C.; Dezayes, C.; Scheiber, J.; Brach, M. Major Geochemical Characteristics of Geothermal Brines from the Upper Rhine Graben Granitic Basement with Constraints on Temperature and Circulation. *Chem. Geol.* **2016**, *428*, 27–47. [CrossRef]
104. Arnórsson, S.; Andrésdóttir, A. Processes Controlling the Distribution of Boron and Chlorine in Natural Waters in Iceland. *Geochim. Et Cosmochim. Acta* **1995**, *59*, 4125–4146. [CrossRef]
105. Burazer, N.; Šajnović, A.; Spahić, D.; Tančić, P.; Grba, N.; Jovančićević, B. Unveiling the Paleosalinity Constraints on Southern Peri-Pannonian Lower Miocene Lacustrine Systems in Serbia and Bosnia and Herzegovina: Lopare (Dinaride Lake System) versus Toplica Basin (Serbian Lake System). *Chem. Geol.* **2025**, *671*, 122475. [CrossRef]
106. Trompetter, W.J.; Reyes, A.G.; Vickridge, I.C.; Markwitz, A. Lithium and Boron Distributions in Geological Samples. *Nucl. Instrum. Methods Phys. Res. Sect. B Beam Interact. Mater. Atoms* **1999**, *158*, 568–574. [CrossRef]
107. Ellis, A.J.; Mahon, W.A.J. *Chemistry and Geothermal Systems*; Denton, J., Ed.; Energy Science and Engineering: Resources, Techonology, Management; Academic Press: New York, NY, USA, 1977.
108. Cinti, D.; Tassi, F.; Procesi, M.; Brusca, L.; Cabassi, J.; Capecchiacci, F.; Delgado Huertas, A.; Galli, G.; Grassa, F.; Vaselli, O.; et al. Geochemistry of Hydrothermal Fluids from the Eastern Sector of the Sabatini Volcanic District (Central Italy). *Appl. Geochem.* **2017**, *84*, 187–201. [CrossRef]
109. Elders, W.A.; Cohen, L.H. Salton Sea Geothermal Field, Imperial Valley, California as a Site for Continental Scientific Drilling. [Abstract Only]. *Geol. Soc. Am. Abstr. Programs* **1983**, *15*.
110. McKibben, M.A.; Williams, A.E.; Elders, W.A.; Eldridge, C.S. Saline Brines and Metallogenesis in a Modern Sediment-Filled Rift: The Salton Sea Geothermal System, California, U.S.A. *Appl. Geochem.* **1987**, *2*, 563–578. [CrossRef]
111. Naidu, G.; Jeong, S.; Johir, M.A.H.; Fane, A.G.; Kandasamy, J.; Vigneswaran, S. Rubidium Extraction from Seawater Brine by an Integrated Membrane Distillation-Selective Sorption System. *Water Res.* **2017**, *123*, 321–331. [CrossRef]
112. Xing, P.; Wang, C.; Chen, Y.; Ma, B. Rubidium Extraction from Mineral and Brine Resources: A Review. *Hydrometallurgy* **2021**, *203*, 105644. [CrossRef]
113. del Villar, A.; Melgarejo, J.; García-López, M.; Fernández-Aracil, P.; Montano, B. The Economic Value of the Extracted Elements from Brine Concentrates of Spanish Desalination Plants. *Desalination* **2023**, *560*, 116678. [CrossRef]